**Corresponding author:**
Maximilian Dröllner;
Email: maximilian.droellner@uni-goettingen.de

**CAMBRIDGE**
UNIVERSITY PRESS

# Multi-method geochronology and isotope geochemistry of carbonatites in the Aileron Province, central Australia

Maximilian Dröllner[1,2] , Christopher L Kirkland[1] , Hugo KH Olierook[1], Andreas Zametzer[1], Bruno V Ribeiro[1,3] , Jonas Kaempf[1], Martin Danišík[4], Bryant Ware[3], Kai Rankenburg[3], David E Kelsey[5], Rose Turnbull[5], Imogen OH Fielding[5], R Hugh Smithies[1,5], Paull Parker[6], Stephanie Wray[6], Andrew Dunn[6] and Kate Vinnicombe[7]

[1]Timescales of Mineral Systems Group, Curtin Frontier Institute for Geoscience Solutions, School of Earth and Planetary Sciences, Curtin University, Perth, WA, Australia; [2]Department of Sedimentology and Environmental Geology, Geoscience Center Göttingen, University of Göttingen, Göttingen, Germany; [3]John de Laeter Centre, Curtin University, Perth, WA, Australia; [4]Western Australia ThermoChronology Facility, John de Laeter Centre, Curtin University, Perth, WA, Australia; [5]Department of Mines, Petroleum and Exploration, Geological Survey of Western Australia, East Perth, WA, Australia; [6]WA1 Resources Ltd, Nedlands, WA, Australia and [7]Encounter Resources Ltd, Subiaco, WA, Australia

## Abstract

Carbonatites are complex rocks yet globally significant hosts of critical mineral resources. Mitigating exploration risk demands robust understanding of their geodynamic setting, which hinges on constraining the timing, duration and nature of associated magmatic and fluid–rock processes. We present multi-method geochronology and isotope geochemistry for the recently discovered Luni and Crean mineralized (Nb, REE, P) carbonatites of the Aileron Province, central Australia. We integrate data from multiple mineral-isotope-pairs: U–Pb and Lu–Hf in zircon, Rb–Sr in biotite and Sr, Lu–Hf, Sm–Nd and (U–Th)/He in apatite. Combined petrological and isotopic evidence resolves distinct geological events over >500 Myr. Zircon U–Pb and biotite Rb–Sr dates range from 831 ± 3 Ma to 796 ± 9 Ma. The oldest dates from less altered minerals reflect primary crystallization, and younger dates relate to pervasive hydrothermal alteration. Radiogenic isotopes (Sr–Nd–Hf) imply a moderately depleted mantle source with negligible recycled sedimentary components in the primary carbonatite magma. Our findings correlate carbonatite magmatism in the Aileron Province at ~830–820 Ma with the onset of Rodinia Supercontinent breakup, during widespread rift-related extension and mantle-derived magmatism across Australia. Post-emplacement, Lu–Hf apatite dates from 722 ± 17 Ma to 653 ± 22 Ma suggest protracted alteration, whereas apatite (U–Th)/He data indicate exhumation at ~250 Ma. Carbonatite emplacement probably exploited pre-existing transcrustal corridors during Tonian extension. These zones of structural weakness likely facilitated ascent of volatile-rich, mantle-derived melts to mid–shallow crustal depths, highlighting how regional geodynamics govern the localization and preservation of mineralized carbonatites.

## 1. Introduction

Carbonatites are complex igneous rocks that frequently host economic deposits of critical metals essential for advanced technologies, especially Niobium (Nb) and rare earth elements (REE) (Mitchell, 2005; Kamenetsky *et al.* 2021; Yaxley *et al.* 2022). Nb, for instance, is a highly strategic metal primarily sourced from carbonatites. Nb is extracted from only three carbonatite locations worldwide, with around 90% of global Nb production coming from a single source, the Araxa mine in Brazil (Mitchell, 2015; Schulz *et al.* 2017; Williams-Jones & Vasyukova, 2023). To understand mineralization drivers in carbonatite systems and, thus, help reduce exploration risk, it is essential to establish their geological timeline and geodynamic context (Hou *et al.* 2015; Williams-Jones & Vasyukova, 2023; Tappe *et al.* 2024). Geochronological and geochemical techniques provide key insights into the origins of carbonatitic melts, their emplacement histories, and post-intrusion alteration systems (Pirajno *et al.* 2014; Downes *et al.* 2016; Yang *et al.* 2017). However, only 64% of known carbonatites have been reliably dated (Humphreys-Williams & Zahirovic, 2021), attesting to the significant challenges in dating the age of primary magmatic crystallization in these rocks. These difficulties arise from several factors, such as secondary alteration processes that overprint original mineral assemblages, the potential cryptic presence of xenocrysts, and the frequent scarcity of zircon for U–Pb geochronology.

Consequently, these challenges often result in ambiguity in the geological interpretation of carbonatite dates (Amelin & Zaitsev, 2002; Millonig et al. 2013; Decrée et al. 2015; Yang et al. 2017; Slezak & Spandler, 2019).

An approach to overcome ambiguity on temporal constraints on lithologies with a complex and/or poly-phased geological history is the integration of multiple isotope systems and minerals, as each mineral–isotope pair has different propensities to growth, resetting or recrystallization under different physico-chemical conditions (Walsh et al. 2013; Slezak & Spandler, 2019; Olierook et al. 2023). Hence, multi-method investigations enable a more holistic temporal framework by potentially tracking processes corresponding to different ambient conditions (e.g. redox state, temperature). In addition to conventional geochronometers, such as U–Pb (Montero et al. 2016; Ghobadi et al. 2018) and Ar–Ar (Madeira et al. 2010), which have been successfully used to date carbonatites, recent advancements in in situ geochronology have expanded the available toolkit. The use of collision and reaction cells in laser ablation inductively coupled plasma mass spectrometry (LA-ICP-MS) now allows for routine in situ Rb–Sr and Lu–Hf dating (Olierook et al. 2020; Simpson et al. 2021; Rösel & Zack, 2022; Simpson et al. 2022; Giuliani et al. 2024; Glorie et al. 2024). Such in situ approaches are particularly advantageous for texturally complex lithologies like carbonatites, as they integrate petrographic context with isotope systematics, enabling spatially-resolved targeting of specific mineral domains within their petrographic context (Vance et al. 2003; Chew et al. 2021; Zametzer et al. 2022; Alfing et al. 2024; Kutzschbach & Glodny, 2024). Beyond age constraints, complementary isotope systems such as Rb–Sr, Sm–Nd and Lu–Hf can further refine information about the source of carbonatitic melts, via initial isotopic ratios (Lee et al. 2006; Tappe et al. 2007; Hou et al. 2015; Oliveira et al. 2017; Tappe et al. 2020; Yaxley et al. 2022). For instance, economic REE enrichment in carbonatites has been linked to Sr and Nd isotopic signatures of sediment recycling (Hou et al. 2015; Hou et al. 2023). Similarly, Nb mineralization is likely controlled by mantle source composition, as carbonated, metasomatically enriched components may contain up to three times more Nb than a primitive mantle source (Williams-Jones & Vasyukova, 2023). Additional insights into the exhumation, cooling and possible alteration history of carbonatites can be gained through low-temperature geochronometers, such as (U–Th)/He thermochronology, which has proven effective for constraining thermal events at shallow crustal levels (Wu et al. 2017; Baughman & Flowers, 2018).

This study presents multi-method geochronological and isotopic data for the recently discovered mineralized (Nb, REE, P) carbonatites in the Western Australian portion of the northern Aileron Province in central Australia (WA1 Resources, 2022a; Fig. 1). The discovery has intensified exploration interest in this area and subsequent drilling campaigns have since confirmed the mineralized nature of the region's carbonatites (WA1 Resources, 2022b; Encounter Resources, 2023; Encounter Resources, 2024), including an total (indicated and inferred) mineral resource estimate for the Luni carbonatite intrusion of $220 \times 10^6$ t at 1.0% $Nb_2O_5$ (WA1 Resources, 2025). These discoveries suggest that the Aileron Province has the potential to rank among the world's most significant Nb resources (Schulz et al. 2017). However, given that carbonatites in this region were identified recently, only preliminary information exists on their timing of emplacement, mineralization history, geodynamic setting and post-emplacement evolution (Kelsey et al. 2024). To investigate these aspects, we analysed a range of mineral-isotope pairs, including zircon for U–Pb and Lu–Hf, biotite for Rb–Sr and apatite for Sr, Lu–Hf, Sm–Nd and (U–Th)/He. By integrating mineral textures and regional context, we test the capability of each pair to capture distinct geological processes in carbonatite systems and interpret the significance of the age and isotope constraints within the broader geodynamic framework that enabled this mineralization.

## 2. Geological background

The Luni and Crean carbonatite intrusions studied in this work are hosted in the Palaeoproterozoic to early Mesoproterozoic (ca. 1860 to 1530 Ma) Aileron Province that is predominantly east–west-trending and situated in central Australia (Fig. 1). The Aileron Province forms the southern part of the North Australian Craton (NAC) and is bounded by the Lasseter Shear Zone to the west and the ca. 1690 to 1600 Ma Warumpi Province to the south (Collins, 1995; Hollis et al. 2013). It remains unclear whether the Warumpi Province is endemic to the Aileron or not, zircon Hf isotope data imply it may reflect a rifted and reattached component (Scrimgeour et al. 2005; Hollis et al. 2013; March et al. 2024). The northern Aileron Province was subjected to peak upper amphibolite and granulite facies metamorphism, dated at ca. 1594 to 1575 Ma within 20 km of the study area (Kelsey et al. 2022; Wingate et al. 2022; Kelsey et al. 2024).

Calcite carbonatite and aillikite lamprophyre intruded Palaeoproterozoic to early Mesoproterozoic granitic, metasedimentary and metagabbronoritic gneisses in the northern Aileron Province during the Neoproterozoic (Kelsey et al. 2024). In addition, from about 60 km south of our study area, Sudholz et al. (2023) reported a perovskite U–Pb age of 806 ± 22 Ma from aillikite-type ultramafic lamprophyres from diatremes emplaced into Neoproterozoic sedimentary rocks of the Centralian Superbasin that unconformably overlies the Aileron Province, in what is called the Webb Province. Sudholz et al. (2023) also document minor occurrences of carbonatite. Aillikite lamprophyres and calcite carbonatite intersected in drillcore and investigated by Kelsey et al. (2024) yielded a range of dates from different chronometers and samples. From lamprophyre, zircon U–Pb dates ranged between 2674 and 684 Ma; and apatite U–Pb yielded a single date of 863 ± 19 Ma. From carbonatite, apatite Lu–Hf yielded an isochron date of 689 ± 47 Ma. Together, these data were interpreted to suggest a maximum crystallization age of ca. 690 Ma for lamprophyre and carbonatite, and that multiple magmatic pulses were likely (Kelsey et al. 2024). However, the broad range of dates hinders an unambiguous interpretation of the geological meaning of these temporal constraints (see Kelsey et al. 2024 for discussion). Regardless, assuming a crystallization age of 800 Ma for comparative purposes, lamprophyres studied by Kelsey et al. (2024) are isotopically similar to those studied by Sudholz et al. (2023) and exhibit positive $\varepsilon Nd_{(t)}$ values between +3.3 and +4.6 with $\varepsilon Hf_{(t)}$ values between +5.6 to +7.2, while $^{87}Sr/^{86}Sr_{(i)}$ are between 0.70359 and 0.70494 (Kelsey et al. 2024). Assuming the same crystallization age of 800 Ma for carbonatite, they have positive $\varepsilon Nd_{(t)}$ between +2.3 and +3.4 and $\varepsilon Hf_{(t)}$ ranging from +3.4 to +7.7, and $^{87}Sr/^{86}Sr_{(i)}$ between 0.70326 and 0.70674 (Kelsey et al. 2024). These similar initial isotope ratios for the lamprophyres and carbonatites imply an isotopically consistent metasomatized peridotite mantle source with limited crustal contamination (Sudholz et al. 2023; Kelsey et al. 2024). Other, more distal
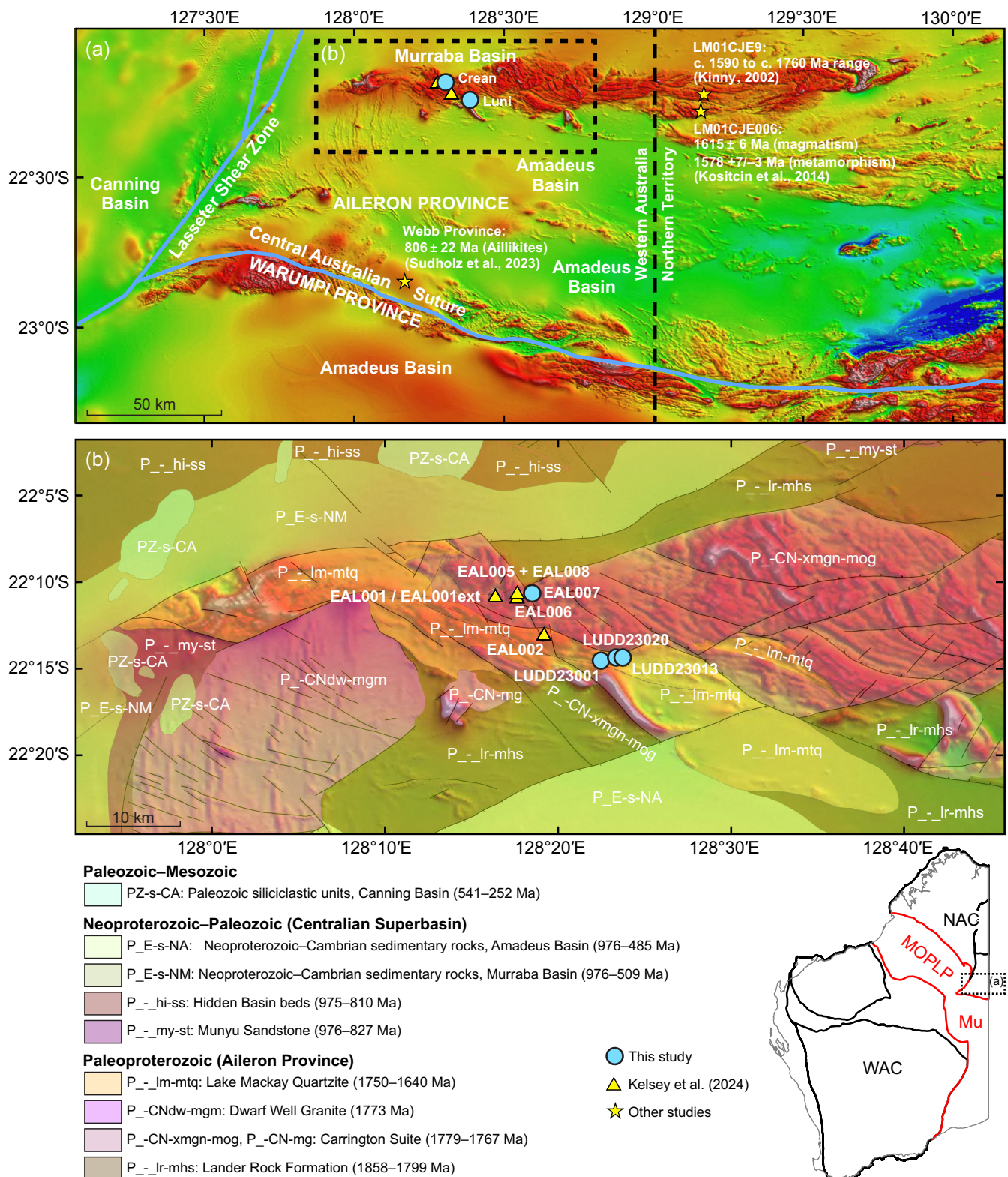
**Figure 1.** (a) Reduced-to-pole magnetic image of the western portion of the Aileron and Warumpi provinces, highlighting the high magnetic intensity belt in the northern Aileron Province some 70–120 km north of the Central Australian Suture. Regions with low magnetic intensity correspond to areas buried by the Centralian Superbasin (Amadeus and Murrabba basins), Canning Basin and regolith. Locations of two geochronology samples from the Rapide Granite in the Northern Territory are indicated (Kinny, 2002; Kositcin et al. 2014). Inset abbreviations: Mu – Musgrave Province; NAC – North Australian Craton; MOPLP – Mirning Ocean–Percival Lakes Province; WAC – West Australian Craton. The black dashed box in the inset marks the main map area. The area labelled "Amadeus Basin" to the north of the Central Australian Suture is along strike to the west of what has been mapped as the Ngalia Basin in the Northern Territory (Edgoose, 2013). (b) Enlargement of the black dashed rectangle in (a), showing the magnetic image with interpreted basement geology and drillcore sample locations (source: https://geoview.dmp.wa.gov.au/geoview/). Figure adapted from Kelsey et al. (2024).

**Table 1.** Collar locations and depths of samples from this study

| Sample ID | Hole ID | Latitude (° S) | Longitude (° E) | Azimuth (°) | Dip (°) | Depth (m) |
|---|---|---|---|---|---|---|
| CWA001 | LUDD23020 | 22.2390 | 128.3896 | 179 | −60 | 82.30–82.55 |
| CWA002 | LUDD23020 | 22.2390 | 128.3896 | 179 | −60 | 88–88.25 |
| CWA004 | LUDD23020 | 22.2390 | 128.3896 | 179 | −60 | 144.8–145.0 |
| CWA006 | LUDD23001 | 22.2426 | 128.3751 | 180 | −60 | 157.9–158.1 |
| CWA003 | LUDD23001 | 22.2426 | 128.3751 | 180 | −60 | 160.75–161.10 |
| CWA005 | LUDD23001 | 22.2426 | 128.3751 | 180 | −60 | 180.5–180.7 |
| CWA007 | LUDD23013 | 22.2380 | 128.3945 | 178 | −60 | 124–124.5 |
| CWA008 | LUDD23013 | 22.2380 | 128.3945 | 178 | −60 | 125–125.25 |
| CWA009 | EAL007 | 22.1768 | 128.3071 | 0 | −60 | 210.05–210.25 |
| CWA010 | EAL007 | 22.1768 | 128.3071 | 0 | −60 | 192–192.3 |

carbonatite occurrences in the Aileron Province include the 731 ± 0.2 Ma Mud Tank carbonatite (Gain *et al.* 2019) and the ca. 1525 Ma Nolans Bore carbonatite (Anenburg *et al.* 2020). The latter shows $^{87}Sr/^{86}Sr_{(i)}$ of ca. 0.7054 and $\varepsilon Nd_{(t)}$ of ca. −4 for unaltered minerals (cf. Huston *et al.* 2016; Anenburg *et al.* 2020), i.e., distinctly different in their isotope compositions compared to data presented by Sudholz *et al.* (2023) and Kelsey *et al.* (2024). Mud Tank apatite grains have $^{87}Sr/^{86}Sr_{(i)}$ of ca. 0.70301 and $\varepsilon Nd_{(t)}$ of ca. +0.25 (Yang *et al.* 2014) that are more similar to the Sr and Nd isotope data from lamprophyres and carbonatites from our study area (Sudholz *et al.* 2023; Kelsey *et al.* 2024). Taken together, the distinct carbonatite ages and varying isotope signatures indicate multiple, spatially and temporally separated episodes of carbonatite emplacement into the Aileron Province and overlying Centralian Superbasin. The study area was also affected by the ca. 610 to 530 Ma Petermann Orogeny (Wade *et al.* 2006; Walsh *et al.* 2013; Ribeiro *et al.* 2023) and the ca. 450–300 Ma Alice Springs Orogeny (Buick *et al.* 2008; Piazolo *et al.* 2020).

## 3. Materials and methods

### 3.a. Sample selection

All recently discovered carbonatite occurrences in the Aileron Province in Western Australia are located in the subsurface, restricting sampling to drillcore material. Understanding of carbonatite genesis in this region is still in its infancy (Kelsey *et al.* 2024), with uncertainties in age relationships between different occurrences and possibly also variability within individual intrusions. To address these uncertainties, we focused on selecting the most promising sections within available drillcores that appeared visually suitable for *in situ* geochronology analyses. Consequently, sampling was not intended to be representative but rather targeted distinct domains with potentially diverse mineralogy to maximize the likelihood of finding minerals suitable for dating. In total, ten samples of carbonatite were selected from recent drilling campaigns, provided by WA1 Resources and Encounter Resources. For the Luni intrusion (WA1 Resources), eight samples were studied from three drillcores (LUDD23001, LUDD23013, LUDD23020), whereas for the Crean intrusion (Encounter Resources), two samples were studied from one

drillcore (EAL007) (Table 1). Although several analysed samples fall outside the strict definition of carbonatite (>50% carbonate minerals), they are genetically related to the carbonatite intrusions. For simplicity, and given that our sampling was not representative in a modal sense, we collectively refer to them as carbonatites.

### 3.b. Sample preparation and imaging

Parts of these drillcores that appeared mineralogically or texturally diverse were selected and cut using a precision saw to prepare polished thin sections, with thin sections prepared at Minerex Services (Esperance, Australia). The remaining material underwent high-voltage pulsed electrical fragmentation using a SelFrag, followed by heavy mineral separation using a heavy liquid (LST FastFloat) with a density of 2.9 g cm⁻³, and magnetic separation using a Frantz isodynamic separator, all at the John de Laeter Centre (JdLC), Curtin University, Perth, Australia. The non-magnetic mineral separates were bulk mounted on double-sided tape, embedded in epoxy resin, ground to approximately half-grain thickness, and polished.

Automated phase identification for all mineral mounts and thin sections was conducted using a Tescan Integrated Mineral Analyzer (TIMA) at the JdLC (Supplementary Text S1). Additional cathodoluminescence (CL) imaging of zircon and apatite was performed using a Tescan Clara field emission scanning electron microscopy (FE-SEM) at the JdLC.

### 3.c. Geochronology and isotope geochemistry

Isotope data were collected at the JdLC, Curtin University. Not all techniques were applied to each sample, but analytical targets were selected to gain broad spatial coverage and to incorporate a range of textural and mineralogical features (Tables 2 and 3). A detailed description of each method is provided in Supplementary Material S1, with a summary provided in the following text. Analyses focused on three geochronometers: zircon, biotite and apatite.

Zircon U–Pb geochronology was conducted for six samples using LA-ICP-MS on polished mineral mounts (Supplementary Text S2). Additionally, split-stream LA-ICP-MS analyses were conducted on two mineral mounts and one thin section to obtain complementary zircon Hf isotope data (Supplementary Text S2). *In situ* Rb–Sr geochronology for biotite was performed on four samples in thin section using LA-ICP-MS with a reaction cell to

**Table 2.** Results of automated phase identification (in vol%) of thin sections analysed via energy dispersive X-ray spectroscopy using the Tescan Integrated Mineral Analyzer (TIMA). Note that the results of thin sections may not fully represent the mineral assemblage of the sampled interval

| Sample ID | CWA001 | CWA002 | CWA004 | CWA006 | CWA003 | CWA005 | CWA007 | CWA008 | CWA010 | CWA009 |
|---|---|---|---|---|---|---|---|---|---|---|
| Hole ID | LUDD23020 | LUDD23020 | LUDD23020 | LUDD23001 | LUDD23001 | LUDD23001 | LUDD23013 | LUDD23013 | EAL007 | EAL007 |
| Quartz | 0.02 | 0.34 | 0.02 | 4.02 | 3.08 | 0.50 | 0.34 | 0.01 | 0.00 | 0.04 |
| Orthoclase | 37.79 | 0.63 | 7.10 | 0.00 | 0.00 | 8.76 | 0.00 | 0.00 | 0.00 | 0.00 |
| Actinolite | 0.00 | 0.00 | 0.00 | 0.00 | 0.01 | 0.00 | 0.01 | 0.01 | 0.15 | 13.38 |
| Aegirine | 0.00 | 0.00 | 0.00 | 0.84 | 0.00 | 0.00 | 0.01 | 0.00 | 1.61 | 3.66 |
| Biotite | 31.64 | 20.97 | 78.99 | 11.21 | 31.62 | 14.51 | 0.01 | 0.00 | 18.07 | 3.93 |
| Calcite | 0.10 | 1.21 | 0.03 | 0.10 | 0.04 | 7.13 | 0.03 | 0.12 | 28.23 | 65.38 |
| Ankerite | 16.14 | 58.91 | 8.27 | 0.07 | 3.24 | 5.04 | 90.44 | 72.86 | 0.17 | 0.16 |
| Gypsum | 0.00 | 0.07 | 0.00 | 36.53 | 38.03 | 44.03 | 0.00 | 0.00 | 0.00 | 0.00 |
| Celestine | 0.01 | 0.08 | 0.00 | 1.34 | 1.31 | 2.53 | 0.01 | 0.00 | 0.08 | 0.08 |
| Apatite | 9.10 | 11.47 | 0.04 | 26.26 | 13.30 | 8.76 | 8.47 | 25.50 | 8.96 | 8.82 |
| Iron oxide | 0.15 | 0.18 | 2.18 | 3.58 | 0.54 | 0.04 | 0.05 | 0.06 | 33.32 | 0.00 |
| Ilmenite | 0.00 | 0.00 | 0.00 | 0.15 | 0.47 | 0.00 | 0.00 | 0.00 | 2.31 | 0.00 |
| Pyrrhotite | 0.00 | 0.00 | 0.00 | 0.07 | 0.05 | 0.00 | 0.01 | 0.00 | 3.20 | 0.01 |
| Pyrite | 0.00 | 0.00 | 0.00 | 0.46 | 1.45 | 0.07 | 0.06 | 0.00 | 0.28 | 0.15 |
| Pyrochlore | 1.52 | 2.64 | 0.11 | 6.63 | 0.90 | 0.18 | 0.01 | 0.00 | 0.87 | 3.25 |
| Unclassified | 0.92 | 2.69 | 1.30 | 6.42 | 4.86 | 7.71 | 0.42 | 1.11 | 2.26 | 0.11 |
| The rest | 2.61 | 0.81 | 1.95 | 2.32 | 1.09 | 0.73 | 0.12 | 0.31 | 0.48 | 1.03 |

**Table 3.** Summary of geochronology and isotope geochemistry results of this study. εHf and εNd calculated at t = 830 Ma. All uncertainties are provided as 2 standard error of the mean

| | | Zircon | | Biotite | Apatite | | | | |
|---|---|---|---|---|---|---|---|---|---|
| Sample ID | Hole ID | U–Pb date (Ma) | εHf$_{(t)}$ | Rb–Sr date (Ma) | $^{87}Sr/^{86}Sr$ | εNd$_{(t)}$ | Sm–Nd date (Ma) | Lu–Hf date (Ma) | (U–Th)/He date (Ma) |
| CWA001 | LUDD23020 | | | | | 4.5 ± 0.5 | 848 ± 36 | 722 ± 17 | |
| CWA002 | LUDD23020 | | | | | | | | |
| CWA004 | LUDD23020 | | 3.5 ± 0.4 | 796 ± 9 | | | | | |
| CWA006 | LUDD23001 | 819 ± 2 | 1.7 to 9.7 | | | 4.6 ± 5.9 | 761 ± 502 | 657 ± 21 | |
| CWA003 | LUDD23001 | | | | | | | | |
| CWA005 | LUDD23001 | | | 819 ± 3 | 0.70296 ± 0.00006 | 4.9 ± 0.8 | 744 ± 69 | 709 ± 18 | |
| CWA007 | LUDD23013 | | | | | | | | |
| CWA008 | LUDD23013 | | | | 0.70284 ± 0.00007 | 6.2 ± 1.4 | 710 ± 109 | 653 ± 22 | 249 ± 13 |
| CWA009 | EAL007 | | | 810 ± 4 | 0.70316 ± 0.00013 | 5.0 ± 2.9 | 754 ± 257 | 686 ± 31 | |
| CWA010 | EAL007 | 813 ± 16 | 6.6 ± 0.9 | 831 ± 3 | 0.70303 ± 0.00016 | 6.7 ± 5.3 | 578 ± 460 | 715 ± 23 | |

resolve isobaric interferences (Supplementary Text S3). Apatite grains were analysed *in situ* with LA-ICP-MS using a reaction cell for temporal constraints via the Lu–Hf system (Supplementary Text S4) and using multicollector-ICP-MS (LA-MC-ICP-MS) for Sm–Nd chronometric and isotopic composition constraints (Supplementary Text S5). The Sr isotopic composition of apatite was measured using thermal ionization mass spectrometry (TIMS)

to determine initial $^{87}Sr/^{86}Sr$ values (Supplementary Text S6). Whereas apatite (U–Th)/He was used to deduce the cooling history of the carbonatite and assess potential recent alteration processes (Supplementary Text S7). Additionally, we selected apatite grains from two samples with distinct mineral assemblage (CWA001 and CWA006) for detailed trace element analysis via laser ablation mapping (Supplementary Text S8).
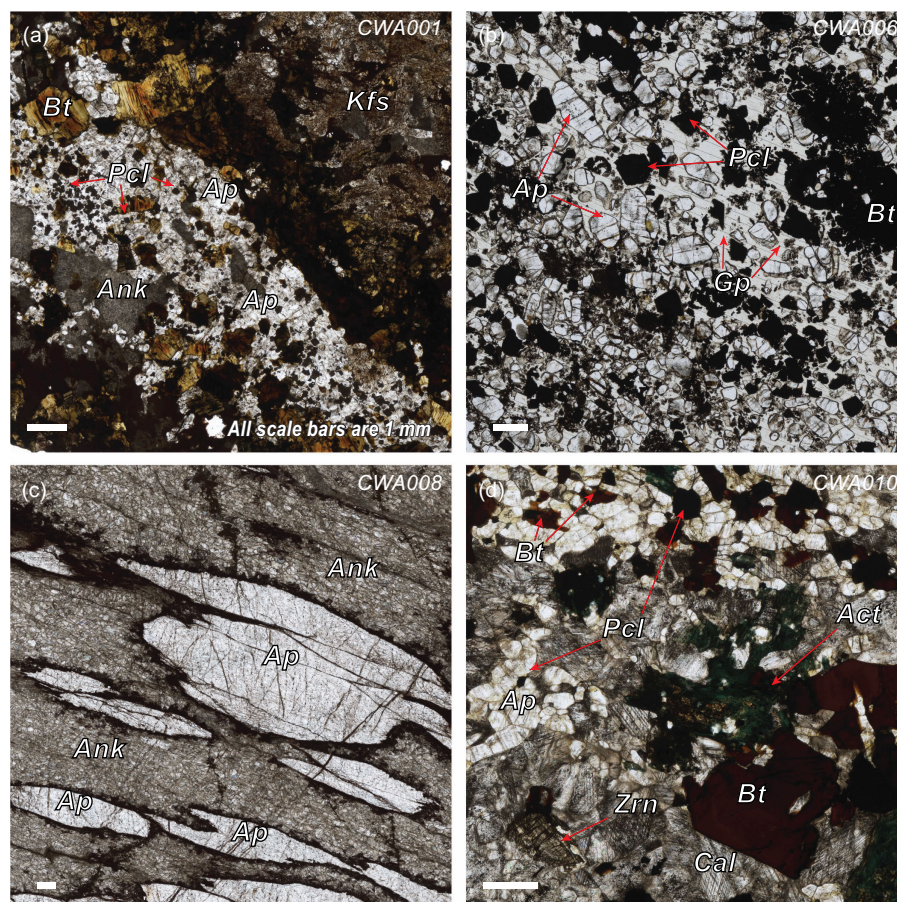
**Figure 2.** Plane-polarized light images of characteristic textures and fabrics observed in optical petrography from samples CWA001 (a), CWA006 (b), CWA008 (c) and CWA010 (d), illustrating the high intra- and inter-sample variability observed in the sample sets investigated herein. Detailed petrographic sample descriptions are provided in the Supplementary Text S9, and false colour mineral maps of all thin sections are provided in the Supplementary Material S1 (Supplementary Figures S1–S10). Ank – ankerite; Act – actinolite; Bt – biotite; Ap – apatite; Bt – biotite; Cal – calcite; Gp – gypsum; Kfs – K-feldspar; Pcl – pyrochlore; Zrn – zircon.

## 4. Results

### 4.a. Mineralogy

Results of automated phase identification are shown in Table 2, and false colour mineral maps of all thin sections are provided in Supplementary Material S1 (Supplementary Figures S1–S10). Optical petrography (Fig. 2) and automated phase identification reveal a highly diverse mineralogy, consistent with the approach to sample selection. While detailed sample descriptions based on optical petrography presenting characteristic features of the samples are provided in Supplementary Text S9, a brief summary is given below and followed by descriptions of mineral textures of target minerals.

Samples CWA001, CWA002 and CWA004 display ankerite as their main carbonate mineral and contain variable amounts of biotite and apatite. Sample CWA001 contains distinct apatite–pyrochlore veins bordered by biotite-rich margins (Fig. 2a) surrounded by K-feldspar. Sample CWA002 is characterized by euhedral biotite sheets (up to 5 mm) that display a distinct core-and-rim zoning, whereas sample CWA004 features abundant (~79%) biotite that possibly reflects replacement of K-feldspar and is intersected by ankerite–magnetite veins. Samples CWA003, CWA005 and CWA006 are characterized by a monomineralic matrix dominated by gypsum, associated with variable amounts of biotite, apatite and minor celestine. Sample CWA003 notably exhibits mineralogically distinct domains enriched in biotite or apatite. Sample CWA005 is distinguished by coarse-grained biotite and K-feldspar phenocrysts in gypsum, while CWA006 contains dispersed apatite, pyrochlore and magnetite within a gypsum

matrix (Fig. 2b). Samples CWA007 and CWA008 share a distinctive texture comprising lens-shaped aggregates of dynamically recrystallized apatite (with internal fabric that is [sub]parallel to the long axis of the lenses) set in polygonally textured ankerite matrices (Fig. 2c). Samples CWA009 and CWA010 contain calcite-dominated matrices with notable occurrences of aegirine, magnetite, apatite and sodic amphibole (Fig. 2d). Sample CWA009 features large aegirine crystals partially replaced by amphibole and biotite, while sample CWA010 is marked by magnetite crystals exhibiting ilmenite exsolution textures and rims of pyrrhotite.

### 4.b. Mineral textures

#### 4.b.1. Zircon

Zircon grains are predominantly anhedral, up to several 100 μm long and abundantly fractured. Their CL response is highly variable within and also between samples (Fig. 3). Samples CWA006, CWA009 and CWA010 contain a small proportion (~10%) of grains that range from well-preserved oscillatory zoned patterns (Fig. 3a–f) to relict magmatic zoning (Fig. 3g, h). The remaining 90% of grains within these three samples, and all grains from CWA001, CWA004 and CWA005, show predominantly chaotic patchy domains within grains (Fig. 3i–l) that largely lack oscillatory zoning. Therefore, almost all zircon grains are characterized by distinct zones that are indicative of secondary processes (e.g. resorption, recrystallization, fluid ingress). Some zircon grains are mantled by euhedral pyrochlore outgrowths (Fig. 3d), whereas others contain inclusions of pyrochlore (Fig. 3l).
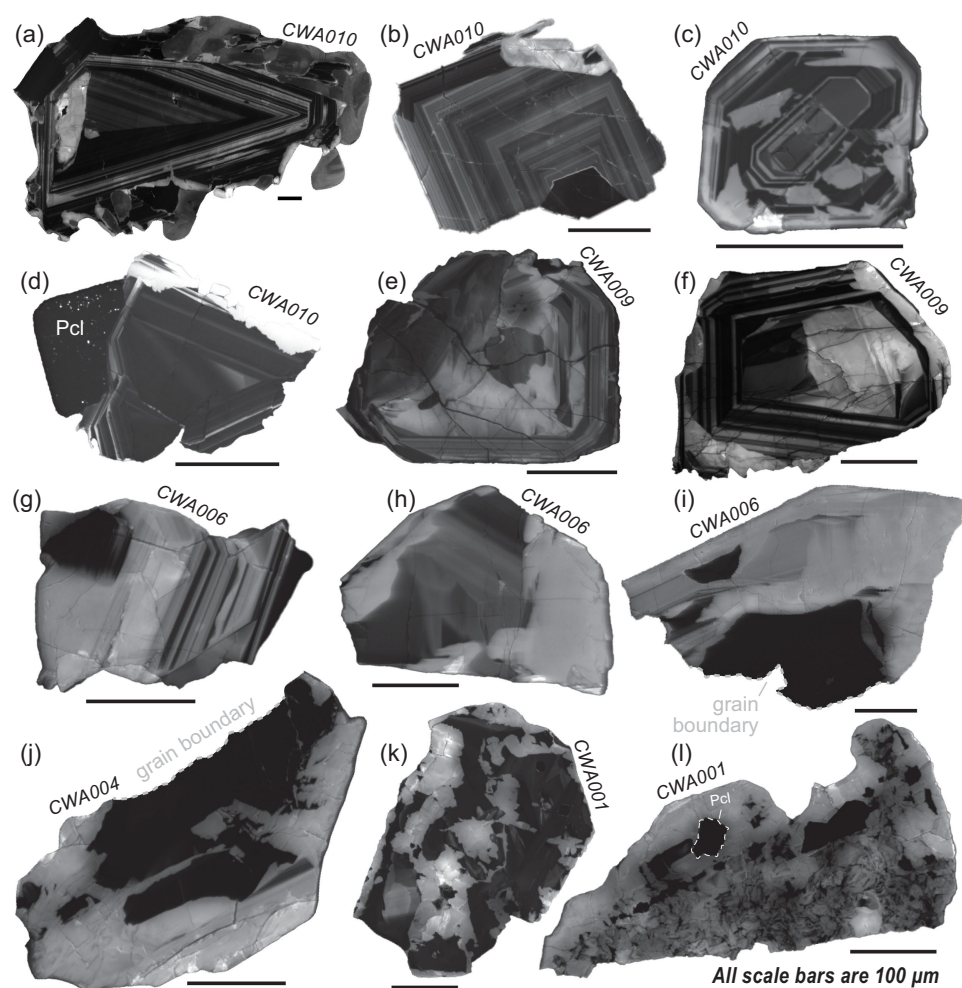
**Figure 3.** Cathodoluminescence images of selected zircon grains from various samples, illustrating different degrees of primary structure modification. The zircon grain in figure part (a) is imaged in thin section, while images (b–l) show grains in mineral mounts. Notably, figure parts (d) and (l) display overgrowths and pyrochlore inclusions, respectively, suggesting a syngenetic relationship between zircon and pyrochlore formation. Dashed grey lines in (i) and (j) mark grain boundaries where the cathodoluminescence response matches that of the background epoxy resin. Pcl – Pyrochlore.

One particularly large zircon grain (>1 mm, Fig. 3a) occurs within the thin section of sample CWA010. This zircon grain contains apatite inclusions, has a seam of external apatite crystals, and is surrounded by a biotite-bearing calcite matrix.

### 4.b.2. Biotite
Biotite typically occurs in different textures in the carbonatite samples. Grains are euhedral to subhedral and, under plane-polarized light, range in colour from translucent to brown (Fig. 4a), pale-brown (Fig. 4b), zoned lighter and darker red–brown (Fig. 4c) and homogenously dark red–brown (Fig. 4d). Parallel lamellae (cleavages) show variable spacing densities, ranging from <10 µm to as wide as ~50 µm (Fig. 4). Mottled textures (Fig. 4a, b) and grain-scale deformation (Fig. 4a, c) are also present.

### 4.b.3. Apatite
Apatite is a major constituent in most samples (Table 2), typically occurring as coarse-grained aggregates or large individual grains, commonly reaching several 100 µm and rarely exceeding 1 mm (Fig. 5a). Many grains exhibit cracks, and CL responses are variable. In samples containing apatite grain aggregates (e.g. CWA001), a grey CL response commonly marks apatite inter-grain boundaries, with thin dark grey veins extending from these boundaries into individual apatite crystals (Fig. 5a). Within these apatite aggregates, pyrochlore crystals are commonly observed, and the surrounding apatite appears to conform to the shape of the pyrochlore inclusions (Fig. 5a). Notably, broad zoning and thin, bright CL veins are visible in several grains (Fig. 5f, g), with the abundance and distribution of these veins varying across samples. Certain samples, such as CWA005 and CWA006, display complex, patchy, chaotic patterns in the central domains of the grains, appearing as bright circular features within a darker core structure (Fig. 5b, d).

Trace element maps shed light on textures observed in CL images, indicating they reflect the distribution of REE and trace elements (e.g. Sr and Y) in individual grains. Apatite from sample CWA001 notably displays a complex chemical zoning, which can be subdivided into three zones based on the light REE (LREE), Sr and Y content (Fig. 5h). For instance, zone 1 resembles a pristine apatite core with higher Sr (10,794 ppm) and LREEs (4817 ppm) compared to zones 2 (8045 ppm Sr; 1176 ppm ΣLREE) and 3 (5946 ppm Sr; 550 ppm ΣLREE), with the latter being the most depleted in LREEs but with higher heavy REE and Y (HREY) (751 ppm ΣHREY) content compared to the other zones (521 and 576 ppm ΣHREY in zone 1 and 2; Fig. 5h). Despite presenting a more homogeneous Mn and Sr composition, apatite from sample
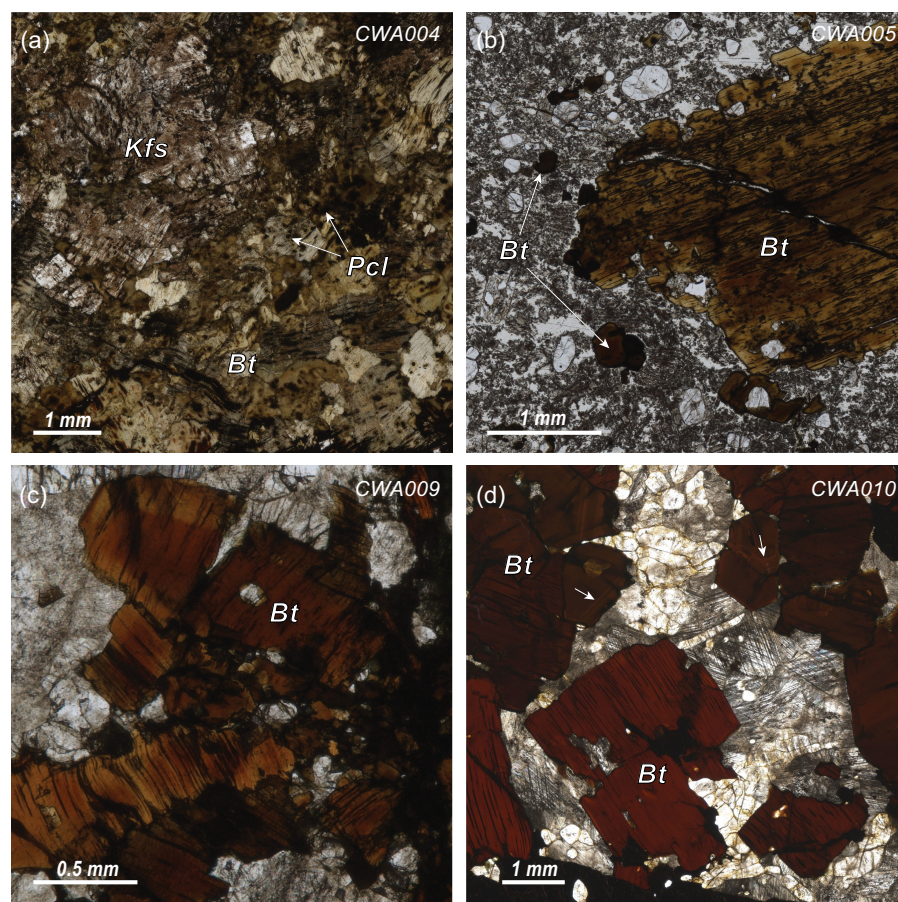
**Figure 4.** Plane-polarized light images of representative biotite textures from samples CWA004 (a), CWA005 (b), CWA009 (c) and CWA010 (d), displaying variations in colour, microstructures and mineral inclusions. Note that biotite in figure panels (b–d) develops euhedral to subhedral sheets with well-preserved oscillatory zoning (white arrows in (d)) indicative of magmatic crystallization, whereas biotite with abundant fine-grained pyrochlore inclusions in (a) replaces former K-feldspar, indicating formation via secondary (metasomatic/hydrothermal) processes. Bt – biotite; Kfs – K-feldspar; Pcl – pyrochlore.

CWA006 also displays multiple zones defined by the variability of Y and REEs, with zone 1 (core) showing an overall higher LREE-HREY content that gradually decreases toward zones 2 and 3 (mantle domains) (Fig. 5i). We note the presence of a narrower rim (zone 4) with higher REE content compared to the other zones.

Chondrite-normalized REE profiles indicate that both apatite cores (zone 1 from CWA001 and CWA006; Fig. 5h, i) are very similar in terms of REE content and LREE-HREY fractionation (Fig. 5j). The apatite LREE variability from CWA001 is reflected in the chondrite-normalized shapes. Zone 1 from CWA001 displays a steep, fractionated profile with $(La/Sm)_{CN}$ of 3.54, whilst zones 2 and 3 show convex profiles with significantly lower $(La/Sm)_{CN}$ of 0.74 and 0.36, respectively, highlighting the LREE depletion compared to zone 1. Apatite from CWA006 displays similar steep, fractionated chondrite-normalized profiles, although with distinct total REE content varying from 4871 ppm (zone 1) to 2687 ppm (zone 3) with a pronounced increase in the rim (zone 4; 6085 ppm). A tabulated dataset with apatite trace element data for the individual areas is provided in Table S1 within the Supplementary Material S2.

### 4.c. Zircon U–Pb geochronology and Lu–Hf isotope geochemistry

In total, 457 U–Pb analyses of 438 zircon crystals (one analysis [$n$] per crystal, except for the large grain in sample CWA010 with $n = 19$ in Fig. 3a) were collected across six samples, with 97 of these from three samples also having complementary Lu–Hf isotopes. The majority of the zircon U–Pb analyses reveal highly scattered and largely discordant data (Fig. S11). Despite the complicated dataset, a significant portion of analyses from two samples (CWA006, CWA010) show clear clustering in U–Pb concordia space (Fig. S11D, F).

Sample CWA006 reveals one concordant cluster of data (defined as a concordia distance between 1.5 and –1.5) and another group that scatters along a trend consistent with loss of radiogenic Pb and some minor to moderate gain of common Pb in some crystals (Fig. S11E). The U and Th contents of zircon analyses of sample CWA006 vary significantly, ranging from very low (U = below detection limit [~2 ppb], Th = 0.6 ppm) to high (U = 624 ppm, Th = 3079 ppm) concentrations. By restricting the near-concordant data cluster to analyses that display moderate to high U concentrations (>5 ppm), a U–Pb concordia date of 819 ± 2 Ma (mean square weighted deviation [MSWD] = 0.25, $p = 0.62$, $n = 21/60$) was derived for sample CWA006 from the Luni intrusion (Fig. S11F).

Sample CWA010 shows a broad cluster of near-concordant data at around 830 Ma for zircon grains analysed in the mineral mount (Fig. S11G). Nonetheless, calculating a reliable weighted mean or concordia age is not warranted due to the dispersed nature of the data, suggesting that processes other than radiogenic decay control much of the isotopic signature of these data. Conversely, the large zircon grain in sample CWA010 (Fig. 3a) was analysed by 19 spot ablations during the split-stream LA-ICP-MS session and provided more consistent results. Using a concordia distance filter of –5 to +5 and discarding one analysis that most likely reflects radiogenic Pb loss (analysis CWA010_TS – 9, Table S2), a relatively imprecise concordia age of 813 ± 16 Ma was calculated (MSWD = 1.2, $p = 0.27$, $n = 8/19$) for the single crystal (Fig. S11H).
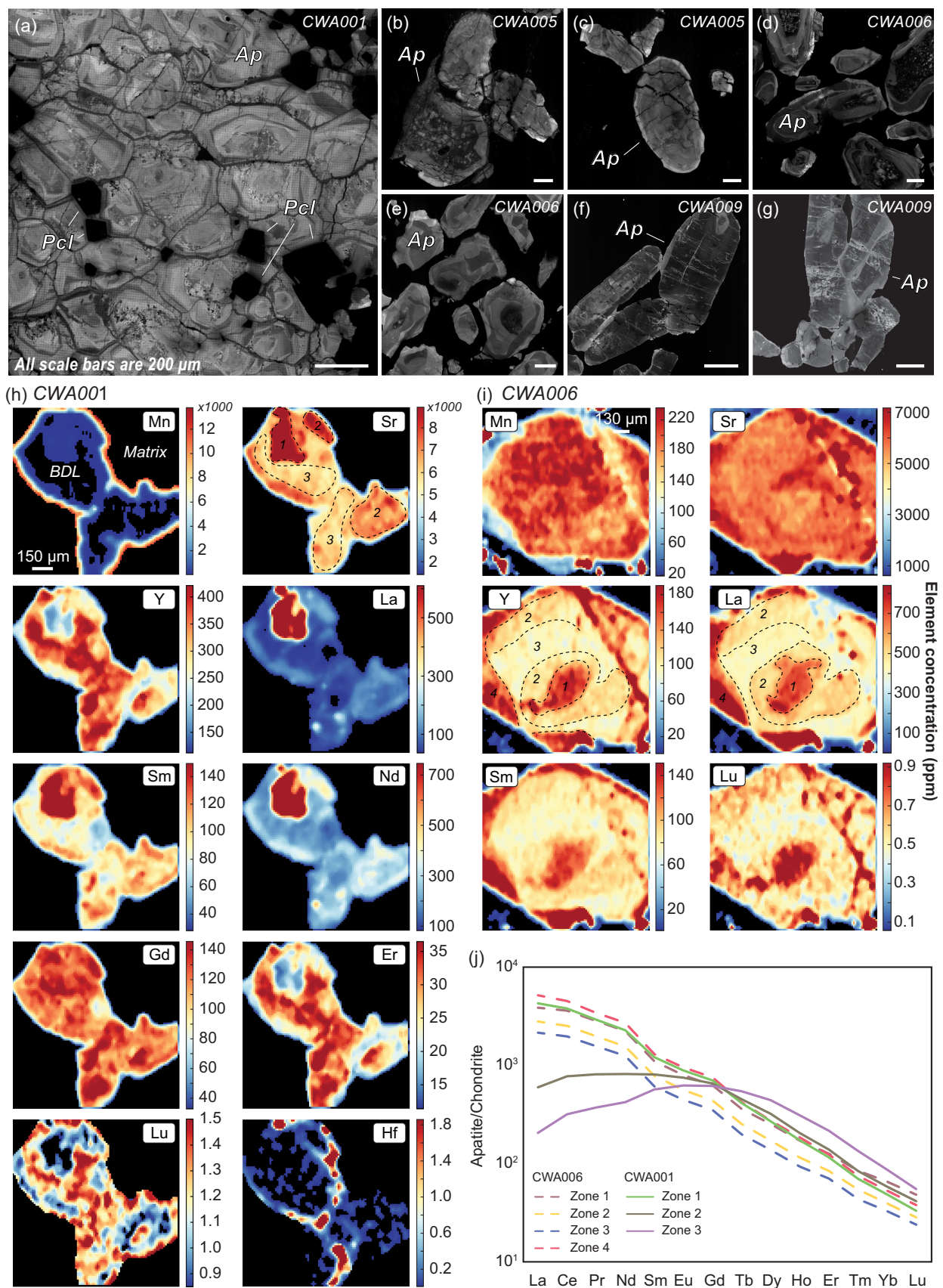
**Figure 5.** (a–g) Cathodoluminescence images of apatite grains highlighting complex apatite internal microstructures and zoning within various samples. In this case, all greyscale features visible are apatite, while other minerals surrounding apatite appear black, i.e., are not cathodoluminescence-active (e.g. pyrochlore in figure part (a)). (h–i) Trace element maps of two apatite grains from sample CWA001 and CWA006 confirm complex chemical zoning of apatite grains. (j) Apatite chondrite-normalized (McDonough & Sun, 1995) REE profiles from the two grains shown in figure part (h) and (i). The abbreviation BDL refers to elements below detection level during trace element mapping via LA-ICP-MS. Colour scales are shown in element concentration (ppm). Ap – Apatite; Pcl – Pyrochlore.

The remaining four samples (CWA001, CWA004, CWA005, CWA009) show extreme scatter on a Tera–Wasserburg U–Pb plot (Fig. S11). Given an absence of a clear trend or concordant data cluster, no robust age information regarding the crystallization of these zircon grains can be extracted. Furthermore, many of the analyses in these four samples exhibited erratic ablation behaviour, indicative of high compositional variability within grains and/or many inclusions.

The complementary Hf isotopic data on the same analytical volume as used for U–Pb geochronology for samples CWA004, CWA006 and CWA010 yielded imprecise Hf isotopic data due to unusually low abundance of Hf. Compared to the reference materials with precision at about 1 $\varepsilon$Hf units, precision for the unknown zircon analyses was typically between 2 and 4 $\varepsilon$Hf (Fig. S12, Table 3). Despite the imprecise data, the Hf isotopic data from the three analysed samples define two distinct, supra-chondritic populations, with no difference between Hf isotopic data for concordant and discordant analyses when back-calculated to 830 Ma (the interpreted age of crystallization, see discussion). Samples CWA004 and CWA010 yielded weighted mean $\varepsilon$Hf$_{(830\ Ma)}$ of +3.5 ± 0.4 (MSWD = 0.78, $p$ = 0.74) and +6.6 ± 0.9 (MSWD = 0.42, $p$ = 0.98), respectively. Sample CWA006 yielded a spread of Hf isotopic data with $\varepsilon$Hf$_{(830\ Ma)}$ from +1.7 ± 2.8 to +9.7 ± 3.7, with individual values encompassing, within uncertainty, both supra-chondritic populations from the other two samples. The complete dataset for U–Pb geochronology and the split-stream (U–Pb, Lu–Hf) sessions is provided in Tables S2 and S3, respectively.

### 4.d. Biotite Rb–Sr geochronology and apatite Sr isotope geochemistry

Biotite Rb–Sr analyses from four samples (CWA004, CWA005, CWA009 and CWA010) document relatively coherent age components as highlighted for both anchored and free-fitted linear regressions (Supplementary Table S4; Fig. S13). Given that biotite and apatite exhibit appearances implying they are likely co-genetic in samples CWA005, CWA009 and CWA010, and because high Sr concentrations in apatite (e.g. ~7000 ppm for CWA009 and CWA010) render disturbance of the Sr isotopic composition during later overprint less problematic, the biotite Rb–Sr age precision may be improved by anchoring to the apatite $^{87}Sr/^{86}Sr$ ratio from the same samples (which should approximate the biotite's initial $^{87}Sr/^{86}Sr_{(i)}$). Measured apatite $^{87}Sr/^{86}Sr_{(i)}$ ratios are consistently unradiogenic (i.e. low $^{87}Sr/^{86}Sr$) and comparable across the different samples (Table 3), yielding 0.70296 ± 0.00006 (CWA005), 0.70284 ± 0.00007 (CWA008), 0.70316 ± 0.00013 (CWA009) and 0.70303 ± 0.00016 (CWA010; Fig. S14). No apatite $^{87}Sr/^{86}Sr$ data was obtained for sample CWA004, which lacks a sufficient number of apatite crystals. Furthermore, textures in CWA004 do not support co-genetic biotite-apatite crystallization. The mean value of the other four samples (0.70294 ± 0.00011, Supplementary Fig. S14) was assumed for sample CWA004. When anchored to apatite initial $^{87}Sr/^{86}Sr$ ratios, inverse biotite Rb–Sr isochrons yield statistically robust (i.e. $p$ > 0.05) dates of 831 ± 3 Ma (CWA010), 819 ± 3 Ma (CWA005), 810 ± 4 Ma (CWA009) and 796 ± 9 Ma (CWA004) (Fig. S13, Table 3). Applying no anchor to sample CWA004 (where co-genetic apatite-biotite is not evident), a free-fitted regression yields a biotite Rb–Sr date of 804 ± 17 Ma. The complete dataset for biotite Rb–Sr geochronology, including dates for free-fitted regressions and conventional isochrons, as well as apatite Sr isotope geochemistry is provided in Tables S4–S6.

### 4.e. Apatite Sm–Nd and Lu–Hf geochronology and isotope geochemistry

Apatite Sm–Nd isotopes from six samples define isochrons but exhibit a large variability of parent–daughter ratios, resulting in different levels of age precision. The most precise temporal constraint is retrieved from sample CWA001, which yielded an apatite Sm–Nd isochron date of 848 ± 36 Ma (MSWD = 1.2, $p$ = 0.09, $n$ = 67). Conversely, other dates are comparably imprecise with 2 standard errors ranging from 9 to 80% (Fig. S15, Table 3). $\varepsilon$Nd$_{(t)}$ values calculated using the initial $^{143}Nd/^{144}Nd_{(i)}$ isochron intercepts range from +4.5 to +6.7 and yielded a weighted mean $\varepsilon$Nd$_{(t)}$ of +4.8 ± 0.4 (MSWD = 1.1, $p$ = 0.34, $n$ = 6).

Apatite Lu–Hf isotopes from six samples define mixing lines between radiogenic and common-Hf components in inverse isochron space (Fig. S16). The isochrons were anchored to an initial $^{177}Hf/^{176}Hf$ of 3.55 ± 0.05 (Spencer *et al.* 2020; Simpson *et al.* 2021), spanning the entire range of initial $^{177}Hf/^{176}Hf$ ratios of the terrestrial reservoir (Spencer *et al.* 2020). Apatite from samples CWA001, CWA005 and CWA010 yields the oldest inverse Lu–Hf isochron dates of 722 ± 17 Ma (MSWD = 1.3, $p$ = 0.10, $n$ = 38), 709 ± 18 Ma (MSWD = 1.2, $p$ = 0.17, $n$ = 44) and 715 ± 23 Ma (MSWD = 1.9, $p$ $\approx$ 0, $n$ = 66), respectively. Conversely, apatite grains from samples CWA006, CWA008 and CWA009 yield younger inverse Lu–Hf isochron dates of 657 ± 21 Ma (MSWD = 1.3, $p$ = 0.10, $n$ = 38), 653 ± 22 Ma (MSWD = 1.2, $p$ = 0.16, $n$ = 47) and 686 ± 31 (MSWD = 1.5, $p$ = 0.01, $n$ = 65), respectively (Fig. S16, Table 3). The complete dataset for biotite Sm–Nd and Lu–Hf geochronology is provided in Tables S7 and S8, respectively.

### 4.f. Apatite (U–Th)/He thermochronology

Apatite (U–Th)/He data collected for sample CWA008 shows very low U concentrations (median = 0.1 ppm) but yields consistent (though slightly overdispersed) He dates with a weighted mean of 249 ± 13 Ma (2SE, MSWD = 3.8, $n$ = 9/10) (Table 3). The complete dataset for apatite (U–Th)/He thermochronology is given in Table S9.

## 5. Discussion

### 5.a. Tonian carbonatite emplacement and implications for Nb mineralization

The dates obtained in this study from different geochronometers range from 831 ± 3 Ma (biotite Rb–Sr) to 249 ± 13 Ma (apatite [U–Th]/He) (Fig. 6). The oldest dates retrieved are from biotite Rb–Sr, zircon U–Pb and apatite Sm–Nd (although imprecise), spanning ca. 830–800 Ma (Fig. 6). These dates are most likely related to the emplacement processes of the carbonatite system, as they are recorded in a diverse range of carbonatitic lithologies across different drillholes, are distinct from the ages of the host rocks (Kelsey *et al.* 2024) and overlap the recently published 806 ± 22 Ma perovskite U–Pb age from aillikite lamprophyre located ~60 km south of the Luni and Crean intrusions (Sudholz *et al.* 2023). A slightly older apatite U–Pb age of 863 ± 19 Ma from lamprophyre in drillcore EAL002 (Caird target), located about 5 km south of drillcore EAL007, also exists (Kelsey *et al.* 2024; Fig. 1). When considered together, these dates can be interpreted to represent (i) distinct episodes of magmatic activity, with multiple pulses of carbonatitic and lamprophyric magmas over a period of up to 60
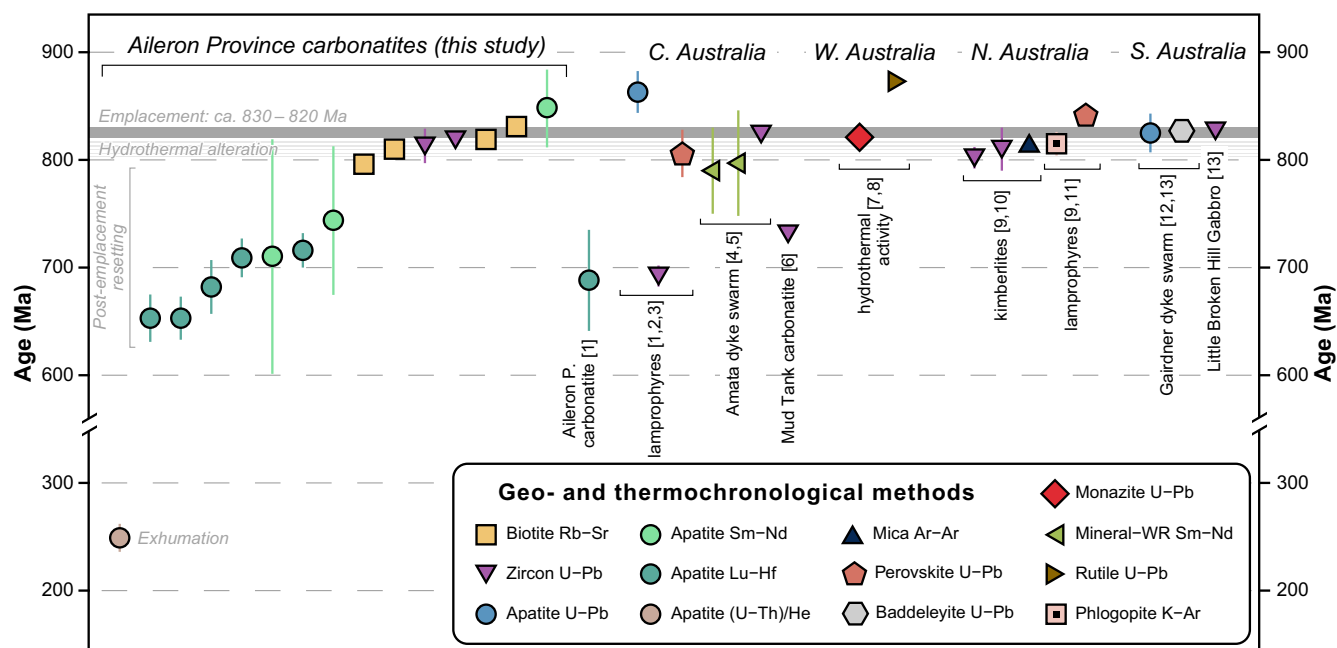
**Figure 6.** Summary of temporal constraints for carbonatites that intruded into the Aileron Province (this study, left side), with a comparison to broadly coeval ages of lithologies in Australia interpreted in the context of extensional events during the breakup of the Rodinia Supercontinent. All uncertainties are 2SE. Note that apatite Sm–Nd dates with uncertainties >20% ELR.2510034 (2SE) are not shown. C. – Central; W. – Western; N. – Northern; S. – Southern; P. – Province. References are indicated by bracketed numbers: 1 – Kelsey *et al.* (2024); 2 – Wingate *et al.* (2024); 3 – Sudholz *et al.* (2023); 4 – Zhao and McCulloch (1993); 5 – Glikson *et al.* (1996); 6 – Gain *et al.* (2019); 7 – Slezak and Spandler (2019); 8 – Olierook *et al.* (2019); 9 – Pidgeon *et al.* (1989); 10 – Downes *et al.* (2007); 11 – Downes *et al.* (2023); 12 – Huang *et al.* (2015); 13 – Wingate *et al.* (1998).

Myr, (ii) variable impacts of post-emplacement modification, or (iii) a combination thereof.

Repeated pulses of emplacement are characteristic of many carbonatite magmatic systems (Decrée *et al.* 2020). While zircon U–Pb dates from both Luni and Crean are within uncertainty (819 ± 2 Ma and 813 ± 16 Ma, respectively) of each other, the biotite Rb–Sr dates show greater spread and less overlap between the intrusions. The 831 ± 3 Ma biotite Rb–Sr date from sample CWA010 at the Crean target predates the zircon U–Pb date and the oldest biotite Rb–Sr date of 819 ± 3 Ma (CWA005) from the Luni deposit, but also the younger biotite Rb–Sr date of 810 ± 4 Ma (CWA009) within the same intrusion. Thus, in addition to possible inter-intrusion age differences suggesting Crean might be ca. 10 Myr older than Luni, significant intra-intrusion discrepancies, as documented by the Rb–Sr dates (Table 3), may support the interpretation that the Aileron Province was intruded by carbonatites (and other low-volume mantle melts) over a prolonged period.

A challenge in interpreting the geological meaning of these dates is the strong textural evidence for hydrothermal alteration (Figs. 3–5). This alteration could either reflect syn-emplacement metasomatic processes (e.g. fenitization) of individual carbonatite pulses, in which case the dates constrain both emplacement and alteration, or late-stage post-magmatic fluid activity, in which case the dates might not represent a prolonged period of carbonatite emplacement. For instance, the texture of biotite across different samples suggests varying degrees of modification, and both deposits each display two distinct biotite dates. Especially, sample CWA010 (Crean), with a biotite Rb–Sr age of 831 ± 3 Ma, appears to preserve euhedral sheets of pristine (magmatic) biotite with oscillatory zoning, showing no signs of post-crystallization modification (Fig. 4d). In contrast, biotite in samples CWA005 (819 ± 3 Ma, Luni) and CWA009 (810 ± 4 Ma, Crean) display

increasing evidence of post-crystallization modification, such as deformation microstructures, irregular intra-grain colour variability and alteration along grain boundaries and cleavage planes. Notably, biotite yielding the youngest Rb–Sr date (796 ± 9 Ma) in sample CWA004 (Luni) forms as monomineralic aggregates (~80 vol.%) replacing former K-feldspar, which we interpret to reflect secondary formation via hydrothermal fluids. As such, biotite from sample CWA010 likely preserves the minimum magmatic crystallization age.

Evidence for modification is also observed in zircon (Fig. 3), but the overlap between zircon U–Pb dates and the oldest biotite Rb–Sr dates from Luni and Crean implies that despite zircon's internal fractures, elevated common Pb, and trends toward higher $^{238}U/^{206}Pb$ ratios (indicating radiogenic Pb loss), a magmatic or xenocrystic component may persist. Specifically, zircon ages of 813 ± 16 Ma at Crean and 819 ± 2 Ma at Luni are consistent with the oldest biotite dates of 831 ± 3 Ma and 819 ± 3 Ma, respectively. The age equivalence at each deposit suggests that while zircon has undergone post-crystallization modification, some primary age information remains, which raises the possibility that the Crean and Luni carbonatite intrusions are not exactly the same age. However, the present data density and the potential for resetting of the zircon U–Pb system do not resolve whether these intrusions were emplaced separately at ca. 831 Ma and ca. 819 Ma or if the younger Luni dates reflect a later minor magmatic pulse or post-emplacement modification of a ca. 831 Ma intrusion.

The older 863 ± 19 Ma apatite U–Pb date from a proximal lamprophyre (Kelsey *et al.* 2024) predates the ca. 830–820 Ma magmatic episode documented in biotite and zircon, and may suggest an earlier onset of low-volume melt generation. However, the relatively small age difference (~10 Ma, considering uncertainties) makes it difficult to confidently distinguish this single lamprophyre date from the tightly clustered dates presented here
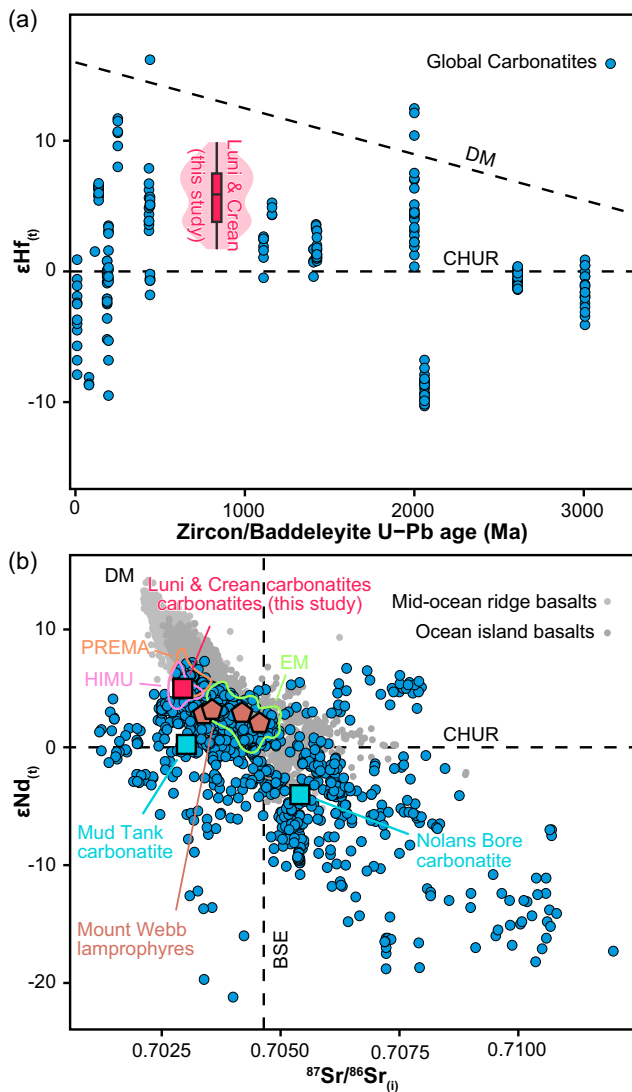
**Figure 7.** (a) Lu–Hf and (b) Sr–Nd compositions of the carbonatites in the Aileron Province region compared to the global compilation of carbonatite (Yaxley *et al.* 2022), the global compilation of basalts (Stracke, 2012) and other localities discussed in this work. BSE – Bulk Silicate Earth; CHUR – CHondritic Uniform Reservoir; DM – Depleted Mantle; EM – Enriched Mantle; HIMU – high-$^{238}U/^{204}Pb$ end-member; PREMA – PREvalent MAntle.

based on simple theoretical considerations. For example, the U–Pb apatite data define a discordia trend in 2D Tera-Wasserburg space, representing a mixing line between common and radiogenic Pb components. This trend includes a tail extending toward high common Pb values and a cluster of analyses with elevated common Pb. These clustered analyses exert an anchoring effect, strongly influencing the lower intercept age. By means of example, excluding certain data points (e.g. those with U < 1 ppm), which retain a single high common Pb analysis (reverse discordant), yields an age within uncertainty of the other putative emplacement ages. A more robust interpretation may be achieved by incorporating the $^{204}Pb/^{206}Pb$ ratio (Ludwig, 1998). However, this approach is technically hampered by the instrumentation used (LA-ICP-MS; Kelsey *et al.* 2024) as it usually requires either multicollector or TIMS analysis, due to the low mass abundance of $^{204}Pb$ and carrier gas Hg interference. Therefore, it currently appears most parsimonious to interpret the apparently slightly older apatite U–Pb date as consistent with a 830–820 Ma magmatic

emplacement, which best constrains initiation of Tonian low-volume mantle melting in the Aileron Province.

Furthermore, all zircon and biotite ages presented here are significantly older than the ~690 Ma zircon U–Pb and apatite Lu–Hf components identified by Kelsey *et al.* (2024) in lamprophyre and carbonatite samples, respectively. Zircon internal structures, truncations observed in CL imagery, grain size, shape and individual spot analyses suggest that all zircon and apatite were xenocrystic, leading Kelsey *et al.* (2024) to infer that magmatic emplacement of both lamprophyre and carbonatite occurred after ca. 690 Ma. While Lu–Hf apatite systematics are likely disturbed (as discussed in Section 5.c) and hence are not suitable to constrain magmatic emplacement, zircon grains analysed in this study interestingly do not display a clear correlation between their textural disturbance and the chances of recording a possibly meaningful geochronological component. Specifically, sample CWA006 exhibits a cluster of near-concordant data (Fig. S11E, F) but shows only faint relics of relict magmatic zoning (Fig. 3g–i). Conversely, data obtained from apparently less disturbed grains (e.g. sample CWA009, Fig. 3e, f) result in considerably more scatter in U–Pb space (Fig. S11). While textural observations offer limited insight into whether the ca. 820 Ma zircon dates are magmatic or result from Pb loss, the large (>1 mm) zircon from Crean is likely not xenocrystic due to its unusual grain size, typical of carbonatitic zircon and its identical date compared to Luni's zircon date. Additionally, biotite's shape, texture and abundance imply it is unlikely to be xenocrystic, and its dates, along with the more cryptic zircon U–Pb data, suggest that magmatic emplacement of carbonatite (and possibly lamprophyre) occurred no later than ca. 830–820 Ma.

Irrespective of whether there is one or multiple pulses of carbonate emplacement, these findings highlight an approximate period of carbonatite magmatic emplacement between 830 and 820 Ma, which likely constrains the timing of primary Nb minerali-zation. Most Nb in the sampled sections is hosted in euhedral pyrochlore crystals (see Supplementary Material S2 and Supplementary Figures S1–S10), suggesting primary igneous crystallization of pyrochlore, with limited remobilization of Nb in the deeper sections of the drillcores, which sampled the relatively unaltered part of the carbonatite intrusions (WA1 Resources, 2024). Furthermore, the occurrence of pyrochlore as both inclusions within and outgrowths on zircon (e.g. Fig. 3d, l) supports broadly coeval crystallization of pyrochlore and zircon.

## 5.b. Emplacement of carbonatites into the Aileron Province during the Rodinia Supercontinent breakup

The mantle beneath the Aileron Province is potentially metal-rich, owing to metasomatic refertilization by silicate–carbonate melts (Sudholz *et al.* 2023). High-temperature fertile melts are expected to be present at both the lithosphere–asthenosphere boundary and deep within the subcontinental lithospheric mantle (Sudholz *et al.* 2023). Whereas our data do not provide direct insights into how deep source melting occurred, the combined Sr–Nd–Hf (Fig. 7) data are broadly consistent with those from the Mount Webb aillikite lamprophyres located ~60 km south of the carbonatite occurrences documented here and believed to be sourced from re-melting of subcontinental lithospheric mantle that became metasomatized by primary asthenospheric carbonate-rich melts (Fig. 7; Sudholz *et al.* 2023). The combined Sr–Nd–Hf data from the carbonatites are more enriched than typical depleted astheno-spheric mantle (e.g. mid-ocean ridge basalts) but slightly less
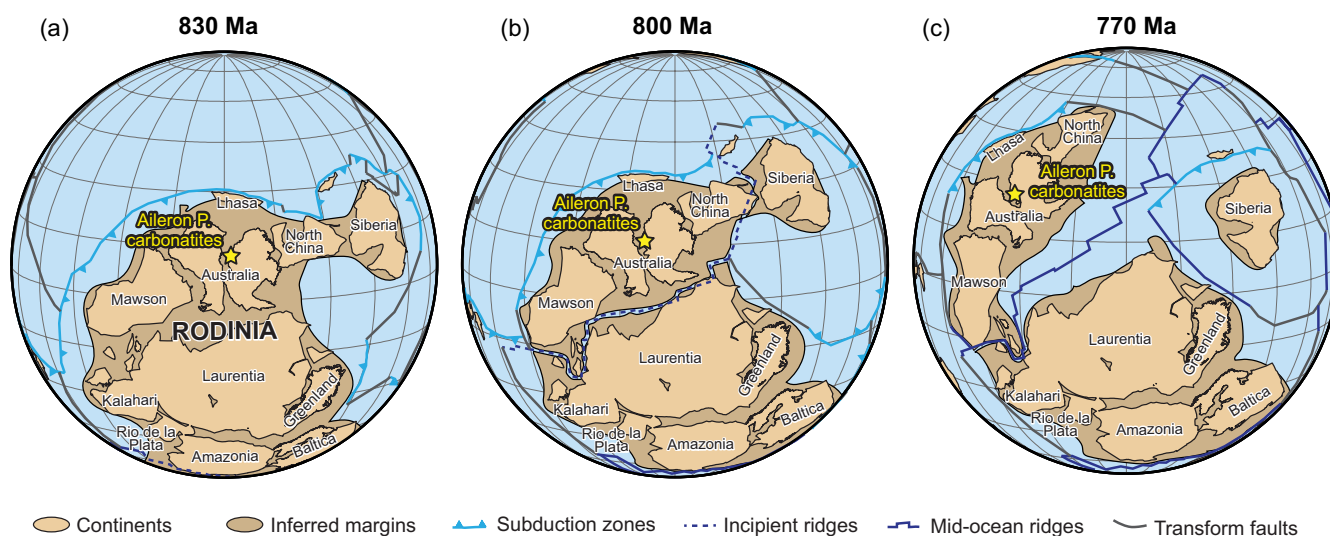
**Figure 8.** (a–c) Palaeogeographic reconstruction during the time of carbonatite emplacement that coincides with the breakup of the Rodinia Supercontinent. Plate reconstructions made using resolved topologies, rotation poles and continent boundaries from Merdith *et al.* (2021) with GPlates v2.5 (Müller *et al.* 2018), projected orthographically with a longitudinal and latitudinal meridian of 120° and 10°N. P. – Province.

enriched than the aillikites. Relatively unradiogenic Sr together with radiogenic Nd and Hf (Fig. 7), and the absence of any clear xenocrystic zircon population (cf. Kelsey *et al.* 2024), suggest that recycled crustal material exerted only a limited influence on both the carbonatite melt source and its ascent. This limited influence may be attributed in part to the low viscosity of the carbonate melt and its immiscibility with the siliceous wall rocks. Although minor heterogeneity in the metasomatic source, such as variations in vein-to-wall-rock ratios or the composition of metasomes, may also contribute to the slight Sr–Nd differences between the samples studied herein and those from previously published proximal lamprophyres and carbonatites (Sudholz *et al.* 2023; Kelsey *et al.* 2024), it is important to note that those earlier data are based on whole-rock analyses, which are more susceptible to alteration and resetting (Hammerli *et al.* 2019; Bruand *et al.* 2023). Moreover, the observed trend toward higher $^{87}Sr/^{86}Sr$ ratios and lower εNd values could reflect some assimilation of crustal material through entrainment that is probably more likely to affect whole-rock data and, without sufficient equilibration, unlikely to be discernible at the mineral scale. However, negligible impact from sediment recycling is also consistent with only a moderate REE enrichment at Luni and Crean, since REE enrichment in carbonatite deposits is typically linked to fertilization by fluids derived from recycled sedimentary material (Hou *et al.* 2015; Hou *et al.* 2023). Additionally, the similarity of isotopic compositions between the Luni and Crean intrusions indicates that the carbonatite melts were likely derived from the same source area, branching into multiple conduits at upper crustal levels, similar to observations in other carbonatite systems (e.g. Bayan Obo; Xue *et al.* 2024).

The geodynamic setting at ca. 830 to 800 Ma provides clues to the mechanisms by which the carbonatite melt was transported from its mantle source to the surface (Fig. 8). By 900 Ma, the Rodinia Supercontinent had assembled and incorporated more than 70% of its continental blocks (Li *et al.* 2008; Merdith *et al.* 2021; Li *et al.* 2023). At this time, southern and northern Australia were joined, with Australia proximal to Laurentia, East Antarctica and the North China and Kalahari cratons. Recent palaeomagnetically constrained,

full plate reconstructions indicate that continental breakup did not occur until 800–780 Ma (Fig. 8), whereby Australia began to break away from Laurentia (Merdith *et al.* 2021; Li *et al.* 2023). However, the period between ca. 870 Ma and 800 Ma was associated with significant extensional events, induced by anticlockwise rotation of the core of the Rodinia Supercontinent (including northern Australia; Merdith *et al.* 2021) and perhaps true polar wander (Li *et al.* 2004). Extension accelerated from ca. 830 Ma onwards, as evidenced by voluminous mafic intrusions and volcanism, including the ca. 830–825 Ma Gairdner–Willouran large igneous province in Australia (Wingate *et al.* 1998; Wang *et al.* 2010) and the ca. 800 Ma Rushinga–Bukoba large igneous province in the Kalahari Craton (Hanson, 2003; Johnson *et al.* 2005). Although it is uncertain whether some other magmatically active blocks were part of the Rodinia Supercontinent, ca. 825 to 800 Ma bimodal magmatism also occurred in the South China (Li *et al.* 2002; Zhou *et al.* 2002; Li *et al.* 2004; Li *et al.* 2005) and Tarim blocks (Liou *et al.* 1996; Chen *et al.* 2004; Zhang *et al.* 2007). Finally, low-volume ca. 830 to 800 Ma volatile-rich mantle-derived products are common across Australia (Fielding & Jaques, 1986; Pidgeon *et al.* 1989; Downes *et al.* 2007; Downes *et al.* 2023; Sudholz *et al.* 2023). The combined magmatic events and sedimentary deposition point to rift-related extension from 830–800 Ma, eventually culminating in the breakup of the Rodinia Supercontinent. Extension facilitated (re)opening of trans-crustal structural discontinuities that could have enabled ascent of carbonatitic melt from the lithospheric mantle, consistent with occurrences of carbonatites proximal to faults (Encounter Resources, 2024). Like many other mantle-derived, volatile-rich products (e.g. kimberlites, lamproites and lamprophyres), extension appears as a leading cause for rapidly transporting carbonate-rich mantle-derived melt to higher crustal levels (Gernon *et al.* 2023; Olierook *et al.* 2023; Sudholz *et al.* 2023). In central Australia, rifting, and potentially elevated mantle potential temperature from nearby plume activity, likely have driven decompression of volatile-bearing, metasomatized peridotite in the deep lithospheric mantle, allowing it to cross its volatile-saturated solidus and generate low-volume, incompatible-element-rich melts. These same processes may explain

both carbonatite formation at Luni and Crean and lamprophyre magmatism (Webb Province; Sudholz et al. 2023), given their temporal and geochemical similarities (Figs. 6 and 7).

Finally, the locations of carbonatite intrusions in the Aileron Province are proximal to the southwestern edge of the North Australian Craton, and the Mirning Ocean–Percival Lakes Province (MOPLP; Kirkland et al. 2017; Lu et al. 2022) that represents a continuous domain of juvenile mid-Proterozoic (ca. 1900–1300 Ma) lithosphere. The MOPLP is mostly deeply buried beneath the Centralian Superbasin and Palaeozoic–Mesozoic Canning Basin but stretches at least as far south as the Proterozoic segment between the Gawler and Yilgarn cratons (Kirkland et al. 2017) and separates the West from North Australian Craton (Lu et al. 2022). The eastern boundary of the North Australian Craton is probably delineated by the north-northeast-trending Lasseter Shear Zone (Kelsey et al. 2022; Martin et al. 2022), located about 60 km west of the sampled carbonatite (Fig. 1A). This transcrustal corridor is evidenced in deep passive and active seismic and magnetotelluric records, which show a strong gradient at the asthenosphere–lithosphere (Doublier et al. 2020; Gorbatov et al. 2020; Duan et al. 2021; Sudholz et al. 2023) and perhaps less strongly at the mantle–crust boundaries (i.e. the Moho; Kennett et al. 2011; Kennett et al. 2023). Seismic gradients indicate juxtaposed blocks of different velocities, and boundaries between such blocks are typically rheologically weaker and prone to re-activation (Sykes, 1978; Busch et al. 1997; Murphy et al. 2024). The carbonatites studied herein, as well as other Australian carbonatites and Neoproterozoic ultramafic mantle-derived products, such as the Mad Gap Yards alnöite (Downes et al. 2023), the Bow Hill dyke (Fielding & Jaques, 1986) and the Webb aillikite province (Sudholz et al. 2023), are situated proximal to major crustal boundaries. Thus, pre-existing rheological weaknesses beneath and proximal to the Aileron Province allowed for the emplacement of carbonatites and ultramafic, mantle-derived products during Tonian extension. Similar controls likely operated at the global scale, as broadly coeval, widespread occurrences of carbonatite and alkaline igneous rocks are well correlated with rifting associated with, and ultimately the breakup of, the Rodinia Supercontinent (Ernst & Bell, 2010). Notable examples occur in former Rodinia fragments, including the Canadian Cordillera (Millonig et al. 2012), the Aillik Bay region of Labrador (Tappe et al. 2006), the Sarfartoq Alkaline Field in Greenland (Tappe et al. 2011), the Arbarastakh Alkaline-Carbonatite Complex and the Beloziminsky Alkaline-Ultrabasic-Carbonatite Massif in Russia (Ashchepkov et al. 2020; Doroshkevich et al. 2022), the Vinoren Aillikite Field in Norway (Zozulya et al. 2020), and the Upper Ruvubu alkaline plutonic complex along the East African Rift (Midende et al. 2014). Collectively, Neoproterozoic rifting and the eventual breakup of the Rodinia Supercontinent appear to mark a global "bloom" of carbonatite and related magmatism, consistent with their frequent occurrences in extensional continental regimes (Humphreys-Williams & Zahirovic, 2021).

## 5.c. Post-Tonian history of carbonatites

The 720–650 Ma apatite Lu–Hf dates are approximately 100 Myr younger than the putative emplacement ages of ca. 830–820 Ma, are similar to a maximum emplacement age interpreted by Kelsey et al. (2024), and younger than the apatite Sm–Nd dates that are broadly consistent with the timing of magmatic crystallization (Fig. 6). This offset, observed within co-genetic minerals from the same sample (e.g. CWA006) and within the same mineral (i.e. Lu–

Hf versus Sm–Nd in sample CWA001), precludes distinct episodes of carbonatite emplacement as the cause but hints at apatite crystallization coeval to magmatic biotite and zircon crystallization at ca. 830–820 Ma. Moreover, the closure temperature of Lu–Hf in apatite (~650–750 °C; Glorie et al. 2024) exceeds that of Rb–Sr in biotite (300–400 °C; Del Moro et al. 1982; Jenkin, 1997), which suggests that neither the cooling history of the carbonatite nor thermal-overprint-driven dry volume diffusion can be invoked to explain the apparent age discrepancy.

Apatite trace element maps from samples CWA001 (Fig. 5h) and CWA006 (Fig. 5i) display preserved cores with higher REE, Mn and Sr content compared to their respective mantle, likely reflecting the primary composition that is surrounded by modified zones with different degrees of trace element depletion. We note that apatite from CWA001 shows a typical LREE depletion trend from zone 1 (core, $\Sigma$LREE = 4817 ppm) to zone 2 and 3 (mantle, 1176 and 550 ppm) often associated with fluid-mediated alteration (Henrichs et al. 2018; Henrichs et al. 2019; Ribeiro et al. 2020), which could reflect the likely late-stage pyrochlore crystallization amidst the apatite texture (Fig. 5a). Despite showing smaller degrees of intra-grain REE depletion (from zone 1 to zone 3), apatite from CWA006 does not display such LREE behaviour likely due to the overall presence of primary euhedral, disseminated pyrochlore that could maintain the REE budget in the sample. Therefore, the observed trace element variations in apatite might reflect post-crystallization hydrothermal alteration directly impacting the REE distribution with potential consequences for Lu–Hf and Sm–Nd geochronometers. Apatite, which is relatively labile to fluid interaction (Harlov & Förster, 2003; Henrichs et al. 2019), may have experienced selective modification in contact with fluids associated with the carbonatite system itself, or during subsequent independent geological events, or a combination of both. Textural observations support fluid-mediated modification, including predominantly anhedral apatite shapes suggesting resorption, CL imaging and trace element maps showing evidence of both primary igneous growth (preserved cores with higher REE, Mn and Sr content), and pervasive modified domains with distinct degrees of REE depletion (Fig. 5). Thus, these textures indicate at least one post-emplacement process that affected the apatite isotopic composition.

A key control on element mobility is not only the presence of fluids, but also the fluid composition (Harlov & Förster, 2003). The fluid's role in preferentially mobilizing Hf over Lu may derive from the different geochemical properties of those elements. High-field-strength elements such as Hf form complexes with halogen-, carbonate-, or sulphate-rich fluids commonly associated with carbonatite systems (Williams-Jones & Migdisov, 2014). By contrast, Lu, Sm and Nd, as REEs ($REE^{3+}$ cations), do not form such strong complexes and may remain incorporated in apatite (Watson & Green, 1981; Fleet & Pan, 1995). This discrepancy could potentially explain the alteration of Lu–Hf isotopic composition while Sm–Nd isotopes in apatite remained unchanged, suggesting fluids capable of mobilizing Hf without dissolving the apatite itself.

The geological control on the Lu–Hf age offset remains unclear, and it may reflect a secondary process unrelated to the carbonatite system and instead be linked to the broader post-carbonatite-emplacement geological history of the Aileron Province. Such a driver could be fluid activity during deposition of Super-sequence 2 in the Centralian Superbasin (from 720 to 650 Ma; Munson et al. 2013). A regional geological control is consistent with similar apatite Lu–Hf dates from farther afield, including 689 ± 47 Ma from calcite

carbonatite in drillcore EAL001ext (Kelsey *et al.* 2024). Moreover, a regional geological event that explains the apatite Lu–Hf dates could also be invoked to explain the cryptic ca. 692 Ma zircon U–Pb population observed in three grains from the lamprophyre dyke in drillcore EAL005. This population has been interpreted as xenocrystic cargo, implying a lamprophyre emplacement after 692 Ma (Kelsey *et al.* 2024). However, if the ca. 692 Ma signal instead resulted from ancient Pb loss, then the more prominent ca. 799 ± 7 Ma population could represent the magmatic crystallization age, which is more consistent with the findings of this study. However, the consistency of the ca. 692 Ma zircon population is not quite in favour of this hypothesis, and ultimately, the geological processes(es) responsible for the apparent resetting of the Lu–Hf apatite system remain ambiguous.

Irrespective of the cause of the resetting of the Lu–Hf isotope system in apatite, the present findings have important implications for the application of apatite Lu–Hf geochronology. Several studies have emphasized the robustness of Lu–Hf in apatite since such ages (retrieved from non-carbonatitic rocks) were regularly found to be identical (within uncertainty) with other high-temperature geochronometers (e.g. zircon), consistent with a relatively high closure temperature of the Lu–Hf system in apatite (Simpson *et al.* 2021; Gillespie *et al.* 2022; Glorie *et al.* 2024). Yet, age discrepancies between zircon and apatite, and between apatite Lu–Hf and Sm–Nd, within carbonatites studied here indicate that the apatite Lu–Hf system (at least when hosted in carbonatites) is prone to fluid-mediated modifications. Hence, in the absence of independent age constraints, detailed grain-scale textural investigations of apatite grains are important to avoid erroneous geological interpretations of apatite Lu–Hf dates. Likewise, placing such textural work within a detailed mineral paragenetic sequence (e.g. Cangelosi *et al.* 2020) based on petrographic studies of well-explored carbonatite systems (i.e. unlike the newly discovered deposits examined here) will help link specific mineral dates to discrete stages of the rock's history. Regardless, the presented CL imaging and trace element mapping appear to be useful tools to resolve primary (preserved cores) and secondary textures that could indicate disturbance of the Lu–Hf systematics (Fig. 5). The isotopic signatures documented here further suggest that mechanisms exist that may decouple the Lu–Hf and Sm–Nd systems in apatite (cf. Gillespie *et al.* 2022), highlighting the need for further studies to identify the underlying drivers.

The apatite (U–Th)/He age of 249 ± 13 Ma is broadly consistent with existing apatite fission track data from (meta)granitoids approximately ≥400 km farther east in the Aileron Province that have central ages that range between 322 ± 15 Ma and 183 ± 8 Ma (Nixon *et al.* 2022). The relatively coherent, albeit slightly overdispersed, thermochronological data may suggest a Permo-Triassic thermal overprint, possibly related to intracontinental fault re-activation along pre-existing structures related to far-field effects from the Tasman Orogen in eastern Australia, as previously argued for the eastern Aileron Province (Nixon *et al.* 2022). However, it may also, or instead, correspond to relatively rapid cooling during denudation of overlying rock during Permian glaciation as discussed for other regions in Australia (e.g. Morón *et al.* 2020). More generally, the (U–Th)/He dates from carbonatite are broadly consistent with the broader regional low-temperature evolution of a range of lithologies in central Australia (Glorie *et al.* 2017; Quentin de Gromard *et al.* 2019). Therefore, the low-temperature history of the carbonatites as recorded in the apatite (U–Th)/He systematics implies a cooling history in tandem with the basement of the region.

## 6. Conclusions

Multi-method geochronology and isotope geochemistry provide a comprehensive framework for understanding the emplacement and evolution of carbonatites intruded into the Aileron Province. Biotite and zircon ages presented in this study define an active Tonian carbonatite system between ca. 830 and 800 Ma. Due to abundant textural evidence for modification in the various target minerals (zircon, biotite, apatite) through hydrothermal alteration, it is argued that the magmatic emplacement period and the related Nb mineralization occurred between ca. 830 and 820 Ma. This period was associated with and/or followed by hydrothermal alteration that pervasively overprinted original magmatic components. The combined Sr–Nd–Hf isotope data presented here indicate that the carbonatites were derived from a metasomatically overprinted, depleted mantle source, consistent with isotopic characteristics of nearby lamprophyres, supporting a shared source region, potentially in the subcontinental lithospheric mantle. The consistent isotopic signatures between two recently discovered Nb-mineralized intrusions, Luni and Crean, further indicate that the melts were derived from the same mantle source and later ascended through multiple conduits at upper crustal levels. The emplacement broadly coincided with the breakup of the Rodinia Supercontinent, when extensional tectonics facilitated melt ascent, possibly through reactivated transcrustal structures along and relatively proximal to major crustal and craton boundaries. A later fluid-mediated modification stage, evidenced by apatite Lu–Hf dates (720–650 Ma) as well as textural and chemical investigations of apatite, indicates post-emplacement alteration, perhaps unrelated to primary carbonatite activity. These findings highlight the importance of integrating multiple geochronological methods and isotopic systems to resolve the complex, multi-phase (and perhaps multi-pulse) histories of carbonatites. Such approaches allow for distinguishing emplacement ages from later alteration events, offering critical insights into the geodynamic and mineralization history of these rocks.

## References

**Alfing J, Johnson TE, Kaempf J, Brown M, Szilas K, Rankenburg K and Clark C** (2024) Eoarchean granulite-facies metamorphism in the Itsaq Gneiss complex, southwest Greenland. *Earth and Planetary Science Letters* **646**, 118977.

**Amelin Y and Zaitsev AN** (2002) Precise geochronology of phoscorites and carbonatites: the critical role of U-series disequilibrium in age interpretations. *Geochimica et Cosmochimica Acta* **66**, 2399–419.

**Anenburg M, Mavrogenes JA and Bennett VC** (2020) The fluorapatite P–REE–Th vein deposit at Nolans Bore: genesis by carbonatite metasomatism. *Journal of Petrology* **61**, egaa003.

Ashchepkov I, Zhmodik S, Belyanin D, Kiseleva ON, Medvedev N, Travin A, Yudin D, Karmanov NS and Downes H (2020) Aillikites and alkali ultramafic lamprophyres of the Beloziminsky alkaline ultrabasic–carbonatite massif: possible origin and relations with ore deposits. *Minerals* **10**, 404.

Baughman JS and Flowers RM (2018) Deciphering a 2 Gyr-long thermal history from a multichronometer (U-Th)/He study of the Phalaborwa carbonatite, Kaapvaal Craton, South Africa. *Geochemistry, Geophysics, Geosystems* **19**, 1581–94.

Bruand E, Storey C, Fowler M, Dhuime B and Doucelance R (2023) Mineral–whole rock isotope fidelity? A comparative study of Hf–Nd–O from high Ba–Sr granitoids. *Chemical Geology* **624**, 121425.

Buick IS, Storkey A and Williams IS (2008) Timing relationships between pegmatite emplacement, metamorphism and deformation during the intra-plate Alice Springs Orogeny, central Australia. *Journal of Metamorphic Geology* **26**, 915–36.

Busch JP, Mezger K and van der Pluijm BA (1997) Suturing and extensional reactivation in the Grenville orogen, Canada. *Geology* **25**, 507–10.

Cangelosi D, Smith M, Banks D and Yardley B (2020) The role of sulfate-rich fluids in heavy rare earth enrichment at the Dashigou carbonatite deposit, Huanglongpu, China. *Mineralogical Magazine* **84**, 65–80.

Chen Y, Xu B, Zhan S and Li Y (2004) First mid-Neoproterozoic paleomagnetic results from the Tarim Basin (NW China) and their geodynamic implications. *Precambrian Research* **133**, 271–81.

Chew D, Drost K, Marsh JH and Petrus JA (2021) LA-ICP-MS imaging in the geosciences and its applications to geochronology. *Chemical Geology* **559**, 119917.

Collins W (1995) Geochronological constraints on orogenic events in the Arunta Inlier: a review. *Precambrian Research* **71**, 315–46.

Decrée S, Savolainen M, Mercadier J, Debaille V, Höhn S, Frimmel H and Baele J-M (2020) Geochemical and spectroscopic investigation of apatite in the Siilinjärvi carbonatite complex: keys to understanding apatite forming processes and assessing potential for rare earth elements. *Applied Geochemistry* **123**, 104778.

Decrée S, Boulvais P, Cobert C, Baele J-M, Midende G, Gardien V, Tack L, Nimpagaritse G and Demaiffe D (2015) Structurally-controlled hydro-thermal alteration in the syntectonic Neoproterozoic Upper Ruvubu alkaline plutonic complex (Burundi): implications for REE and HFSE mobilities. *Precambrian Research* **269**, 281–95.

Del Moro A, Puxeddu M, Di Brozolo FR and Villa IM (1982) Rb–Sr and K–Ar ages on minerals at temperatures of 300–400 °C from deep wells in the Larderello geothermal field (Italy). *Contributions to Mineralogy and Petrology* **81**, 340–49.

Doroshkevich A, Prokopyev I, Kruk M, Sharygin V, Izbrodin I, Starikova A, Ponomarchuk A, Izokh A and Nugumanova Y (2022) Age and petrogenesis of ultramafic lamprophyres of the Arbarastakh alkaline–carbonatite complex, Aldan–Stanovoy Shield, south of Siberian Craton (Russia): evidence for ultramafic lamprophyre–carbonatite link. *Journal of Petrology* **63**, egac073.

Doublier MP, Kennett BLN, Fomin T, Costelloe RD, Moro P, Kohanpour F, Calvert AJ, Huston DL, Champion DC and Southby C (2020) *Basement Architecture from the Pilbara Craton to the Aileron Province: New Insights from Deep Seismic Reflection Line 18GA-KB1*. Canberra: Geoscience Australia.

Downes PJ, Jaques AL, Talavera C, Griffin WL, Gain SEM, Evans NJ, Taylor WR and Verrall M (2023) Perovskite geochronology and petrogenesis of the Neoproterozoic Mad Gap Yards ultramafic lamprophyre dykes, East Kimberley region, Western Australia. *Contributions to Mineralogy and Petrology* **178**, 21.

Downes PJ, Dunkley DJ, Fletcher IR, McNaughton NJ, Rasmussen B, Jaques AL, Verrall M and Sweetapple MT (2016) Zirconolite, zircon and monazite-(Ce) U–Th–Pb age constraints on the emplacement, deformation and alteration history of the Cummins Range Carbonatite Complex, Halls Creek Orogen, Kimberley region, Western Australia. *Mineralogy and Petrology* **110**, 199–222.

Downes PJ, Griffin BJ and Griffin WL (2007) Mineral chemistry and zircon geochronology of xenocrysts and altered mantle and crustal xenoliths from the Aries micaceous kimberlite: constraints on the composition and age of the central Kimberley Craton, Western Australia. *Lithos* **93**, 175–98.

Duan J, Kyi D and Jiang W (2021) *Electrical Resistivity Structures and Mineral Prospectivity from Exploring for the Future AusLAMP Data (2016–2019) in Northern Australia*. Canberra, Australia: Geoscience Australia.

Edgoose CJ (2013) Chapter 24: Ngalia Basin, 1–25. In *Geology and Mineral Resources of the Northern Territory* (eds M Ahmad and TJ Munson). Darwin: Northern Territory Geological Survey Special Publication.

Encounter Resources (2024) *Enriched Niobium Oxide Mineralisation at Aileron – West Arunta: ASX Announcement, 14 October 2024*. Subiaco, WA: Encounter Resources Ltd.

Encounter Resources (2023) *Mineralised Carbonatites Intersected Over 3.5 km West Arunta: ASX Announcement, 28 June 2023*. Subiaco, WA: Encounter Resources Ltd.

Ernst RE and Bell K (2010) Large igneous provinces (LIPs) and carbonatites. *Mineralogy and Petrology* **98**, 55–76.

Fielding DC and Jaques AL (1986) Geology, petrology and geochemistry of the Bow Hill lamprophyre dykes, Western Australia. *International Kimberlite Conference: Extended Abstracts* **4**, 24–26.

Fleet ME and Pan Y (1995) Site preference of rare earth elements in fluorapatite. *American Mineralogist* **80**, 329–35.

Gain SEM, Gréau Y, Henry H, Belousova E, Dainis I, Griffin WL and O'Reilly SY (2019) Mud Tank Zircon: long-term evaluation of a reference material for U-Pb dating, Hf-isotope analysis and trace element analysis. *Geostandards and Geoanalytical Research* **43**, 339–54.

Gernon TM, Jones SM, Brune S, Hincks TK, Palmer MR, Schumacher JC, Primiceri RM, Field M, Griffin WL and O'Reilly SY (2023) Rift-induced disruption of cratonic keels drives kimberlite volcanism. *Nature* **620**, 344–50.

Ghobadi M, Gerdes A, Kogarko L, Hoefer H and Brey G (2018) In situ LA-ICPMS isotopic and geochronological studies on carbonatites and phoscorites from the Guli Massif, Maymecha-Kotuy, Polar Siberia. *Geochemistry International* **56**, 766–83.

Gillespie J, Kirkland CL, Kinny PD, Simpson A, Glorie S and Rankenburg K (2022) Lu–Hf, Sm–Nd, and U–Pb isotopic coupling and decoupling in apatite. *Geochimica et Cosmochimica Acta* **338**, 121–35.

Giuliani A, Oesch S, Guillong M and Howarth GH (2024) Mica Rb-Sr dating by laser ablation ICP-MS/MS using an isochronous calibration material and application to West African kimberlites. *Chemical Geology* **649**, 121982.

Glikson AY, Stewart AJ, Ballhaus CG, Clarke GL, Feeken E, Leven JH, Shearaton JW and Sun S-S (1996) *Geology of the Western Musgrave Block, Central Australia, with Particular Reference to the Mafic-Ultramafic Giles Complex*. Canberra: Australian Government Publishing Service.

Glorie S, Hand M, Mulder J, Simpson A, Emo RB, Kamber B, Fernie N, Nixon A and Gilbert S (2024) Robust laser ablation Lu–Hf dating of apatite: an empirical evaluation. *Geological Society, London, Special Publications* **537**, 165–84.

Glorie S, Agostino K, Dutch R, Pawley M, Hall J, Danišík M, Evans NJ and Collins AS (2017) Thermal history and differential exhumation across the Eastern Musgrave Province, South Australia: insights from low-temperature thermochronology. *Tectonophysics* **703–704**, 23–41.

Gorbatov A, Hejrani B, Zhang F, Medlin A, Costelloe M, Bugden C, Kennett BLN, Am Reading Rawlinson N and Dentith MC (2020) *AusArray: Quality Passive Seismic Data to Underpin Updatable National Velocity Models of the Lithosphere*. Canberra: Geoscience Australia.

Hammerli J, Kemp AI and Whitehouse MJ (2019) In situ trace element and Sm-Nd isotope analysis of accessory minerals in an Eoarchean tonalitic gneiss from Greenland: implications for Hf and Nd isotope decoupling in Earth's ancient rocks. *Chemical Geology* **524**, 394–405.

Hanson RE (2003) Proterozoic geochronology and tectonic evolution of southern Africa. *Geological Society, London, Special Publications* **206**, 427–63.

Harlov DE and Förster H-J (2003) Fluid-induced nucleation of (Y+ REE)-phosphate minerals within apatite: nature and experiment. Part II. Fluorapatite. *American Mineralogist* **88**, 1209–29.

Henrichs IA, Chew DM, O'Sullivan GJ, Mark C, McKenna C and Guyett P (2019) Trace element (Mn-Sr-Y-Th-REE) and U-Pb isotope systematics of metapelitic apatite during progressive greenschist- to amphibolite-facies Barrovian metamorphism. *Geochemistry, Geophysics, Geosystems* **20**, 4103–29.

Henrichs IA, O'Sullivan G, Chew DM, Mark C, Babechuk MG, McKenna C and Emo R (2018) The trace element and U-Pb systematics of metamorphic apatite. *Chemical Geology* **483**, 218–38.

**Hollis JA, Kirkland CL, Spaggiari CV, Tyler IM, Haines PW, Wingate MTD, Belousova EA and Murphy RC** (2013) Zircon U–Pb–Hf isotope evidence for links between the Warumpi and Aileron provinces, west Arunta region. *GSWA Record* **9**, 30.

**Hou Z, Liu Y, Tian S, Yang Z and Xie Y** (2015) Formation of carbonatite-related giant rare-earth-element deposits by the recycling of marine sediments. *Scientific Reports* **5**, 10231.

**Hou Z-Q, Xu B, Zhang H, Zheng Y-C, Wang R, Liu Y, Miao Z, Gao L, Zhao Z, Griffin WL and O'Reilly SY** (2023) Refertilized continental root controls the formation of the Mianning–Dechang carbonatite-associated rare-earth-element ore system. *Communications Earth & Environment* **4**, 293.

**Huang Q, Kamenetsky VS, McPhie J, Ehrig K, Meffre S, Maas R, Thompson J, Kamenetsky M, Chambefort I, Apukhtina O and Hu Y** (2015) Neoproterozoic (ca. 820–830 Ma) mafic dykes at Olympic Dam, South Australia: links with the Gairdner Large Igneous Province. *Precambrian Research* **271**, 160–72.

**Humphreys-Williams ER and Zahirovic S** (2021) Carbonatites and global tectonics. *Elements* **17**, 339–44.

**Huston DL, Maas R, Cross A, Hussey KJ, Mernagh TP, Fraser G and Champion DC** (2016) The Nolans Bore rare-earth element-phosphorus-uranium mineral system: geology, origin and post-depositional modifications. *Mineralium Deposita* **51**, 797–822.

**Jenkin GRT** (1997) Geology: do cooling paths derived from mica Rb-Sr data reflect true cooling paths? *Geology* **25**, 907–10.

**Johnson SP, Rivers T and de Waele B** (2005) A review of the Mesoproterozoic to early Palaeozoic magmatic and tectonothermal history of south–central Africa: implications for Rodinia and Gondwana. *Journal of the Geological Society* **162**, 433–50.

**Kamenetsky VS, Doroshkevich AG, Elliott HAL and Zaitsev AN** (2021) Carbonatites: contrasting, complex, and controversial. *Elements* **17**, 307–14.

**Kelsey DE, Fielding I, Wingate MTD, Smithies RH, Turnbull RE, Ribeiro BV, Maas R, Kirkland CL, Goemann K, Romano SS and Dröllner M** (2024) *Carbonatite, Aillikite Lamprophyre and Host Rocks in the Northern Aileron Province.* Perth: Geological Survey of Western Australia, Record 2024/5, pp. 43.

**Kelsey DE, Korhonen FJ, Romano SS and Spaggiari CV** (2022) *243071: Garnet-Bearing Sillimanite–Magnetite Pelitic Schist, Radiator Prospect.* Perth: Geological Survey of Western Australia.

**Kennett BL, Salmon M, Saygin E and AusMoho Working Group** (2011) AusMoho: the variation of Moho depth in Australia. *Geophysical Journal International* **187**, 946–58.

**Kennett BLN, Gorbatov A, Yuan H, Agrawal S, Murdie R, Doublier MP, Eakin CM, Miller MS, Zhao L and Czarnota K** (2023) Refining the Moho across the Australian continent. *Geophysical Journal International* **233**, 1863–77.

**Kinny PD** (2002) *SHRIMP U-Pb Geochronology of Arunta Province Samples from the Mount Liebig and Lake Mackay 1:250 000 Mapsheets.* Darwin: Northern Territory Geological Survey.

**Kirkland CL, Smithies RH, Spaggiari CV, Wingate MT, Gromard RQ, Clark C, Gardiner NJ and Belousova EA** (2017) Proterozoic crustal evolution of the Eucla basement, Australia: implications for destruction of oceanic crust during emergence of Nuna. *Lithos* **278**, 427–44.

**Kositcin N, Beyer EE and Whelan JA** (2014) *Summary of Results. Joint NTGS–GA SHRIMP Geochronology Project: Arunta Region, July 2013–June 2014.* Darwin, Northern Territory: Northern Territory Geological Survey.

**Kutzschbach M and Glodny J** (2024) LA-ICP-MS/MS-based Rb–Sr isotope mapping for geochronology. *Journal of Analytical Atomic Spectrometry* **39**, 455–77.

**Lee MJ, Lee JI, Do Hur S, Kim Y, Moutte J and Balaganskaya E** (2006) Sr–Nd–Pb isotopic compositions of the Kovdor phoscorite–carbonatite complex, Kola Peninsula, NW Russia. *Lithos* **91**, 250–61.

**Li XH, Su L, Chung S-L, Li Z-X, Liu Y, Song B and Liu DY** (2005) Formation of the Jinchuan ultramafic intrusion and the world's third largest Ni-Cu sulfide deposit: associated with the ~825 Ma South China mantle plume? *Geochemistry, Geophysics, Geosystems* **6**, 1–16.

**Li X-H, Li Z-X, Zhou H, Liu Y and Kinny PD** (2002) U–Pb zircon geochronology, geochemistry and Nd isotopic study of Neoproterozoic bimodal volcanic rocks in the Kangdian Rift of South China: implications for the initial rifting of Rodinia. *Precambrian Research* **113**, 135–54.

**Li Z-X, Liu Y and Ernst R** (2023) A dynamic 2000–540 Ma Earth history: from cratonic amalgamation to the age of supercontinent cycle. *Earth-Science Reviews* **238**, 104336.

**Li Z-X, Bogdanova S, Collins AS, Davidson A, de Waele B, Ernst RE, Fitzsimons IC, Fuck RA, Gladkochub DP and Jacobs J** (2008) Assembly, configuration, and break-up history of Rodinia: a synthesis. *Precambrian Research* **160**, 179–210.

**Li Z-X, Evans DA and Zhang S** (2004) A 90 spin on Rodinia: possible causal links between the Neoproterozoic supercontinent, superplume, true polar wander and low-latitude glaciation. *Earth and Planetary Science Letters* **220**, 409–21.

**Liou JG, Graham SA, Maruyama S and Zhang RY** (1996) Characteristics and tectonic significance of the Late Proterozoic Aksu blueschists and diabasic dikes, Northwest Xinjiang, China. *International Geology Review* **38**, 228–44.

**Lu Y, Wingate MTD, Smithies RH, Gessner K, Johnson SP, Kemp AIS, Kelsey DE, Haines PW, Martin DM and Martin L** (2022) Preserved intercratonic lithosphere reveals Proterozoic assembly of Australia. *Geology* **50**, 1202–07.

**Ludwig KR** (1998) On the treatment of concordant uranium-lead ages. *Geochimica et Cosmochimica Acta* **62**, 665–76.

**Madeira J, Mata J, Mourão C, Da Brum Silveira A, Martins S, Ramalho R and Hoffmann DL** (2010) Volcano-stratigraphic and structural evolution of Brava Island (Cape Verde) based on 40Ar/39Ar, U–Th and field constraints. *Journal of Volcanology and Geothermal Research* **196**, 219–35.

**March S, Hand M, Morrissey L and Kelsey D** (2024) Extension during the Liebig Orogeny: revised tectonic setting of Paleoproterozoic central Australia. *Gondwana Research* **134**, 365–84.

**Martin D, Murdie RE, de Kelsey Q, de Gromard R, Thomas CM, Cutten HN, Zhan Y, Lu Y, Haines PW and Brett J** (2022) Compilation and geological implications of the major crustal boundaries map and 3D model of Western Australia. *Geological Survey of Western Australia: Record* **2022**, 49.

**McDonough WF and Sun S-S** (1995) The composition of the Earth. *Chemical Geology* **120**, 223–53.

**Merdith AS, Williams SE, Collins AS, Tetley MG, Mulder JA, Blades ML, Young A, Armistead SE, Cannon J and Zahirovic S** (2021) Extending full-plate tectonic models into deep time: linking the Neoproterozoic and the Phanerozoic. *Earth-Science Reviews* **214**, 103477.

**Midende G, Boulvais P, Tack L, Melcher F, Gerdes A, Dewaele S, Demaiffe D and Decrée S** (2014) Petrography, geochemistry and U–Pb zircon age of the Matongo carbonatite Massif (Burundi): implication for the Neoproterozoic geodynamic evolution of Central Africa. *Journal of African Earth Sciences* **100**, 656–74.

**Millonig LJ, Gerdes A and Groat LA** (2013) The effect of amphibolite facies metamorphism on the U–Th–Pb geochronology of accessory minerals from meta-carbonatites and associated meta-alkaline rocks. *Chemical Geology* **353**, 199–209.

**Millonig LJ, Gerdes A and Groat LA** (2012) U–Th–Pb geochronology of meta-carbonatites and meta-alkaline rocks in the southern Canadian Cordillera: a geodynamic perspective. *Lithos* **152**, 202–17.

**Mitchell RH** (2015) Primary and secondary niobium mineral deposits associated with carbonatites. *Ore Geology Reviews* **64**, 626–41.

**Mitchell RH** (2005) Carbonatites and carbonatites and carbonatites. *The Canadian Mineralogist* **43**, 2049–68.

**Montero P, Haissen F, Mouttaqi A, Molina JF, Errami A, Sadki O, Cambeses A and Bea F** (2016) Contrasting SHRIMP U–Pb zircon ages of two carbonatite complexes from the peri-cratonic terranes of the Reguibat Shield: implications for the lateral extension of the West African Craton. *Gondwana Research* **38**, 238–50.

**Morón S, Kohn BP, Beucher R, Mackintosh V, Cawood PA, Moresi L and Gallagher SJ** (2020) Denuding a craton: thermochronology record of phanerozoic unroofing from the Pilbara Craton, Australia. *Tectonics* **39**, e2019TC005988.

**Müller RD, Cannon J, Qin X, Watson RJ, Gurnis M, Williams S, Pfaffelmoser T, Seton M, Russell SHJ and Zahirovic S** (2018) GPlates: building a virtual Earth through deep time. *Geochemistry, Geophysics, Geosystems* **19**, 2243–61.

**Munson TJ, Kruse PD and Ahmad M** (2013) Chapter 22: centralian superbasin. In *Geology and Mineral Resources of the Northern Territory*. Darwin: Northern Territory Geological Survey.

**Murphy BS, DeLucia MS, Marshak S, Ravat D and Bedrosian PA** (2024) Magnetotelluric insights into the formation and reactivation of trans-crustal shear zones in Precambrian basement of the eastern US Midcontinent. *Bulletin* **136**, 2661–75.

**Nixon AL, Glorie S, Fernie N, Hand M, van Vries Leeuwen AT, Collins AS, Hasterok D and Fraser G** (2022) Intracontinental fault reactivation in high heat production areas of central Australia: insights from apatite fission track thermochronology. *Geochemistry, Geophysics, Geosystems* **23**, e2022GC010559.

**Olierook HKH, Fougerouse D, Doucet LS, Liu Y, Rayner MJ, Danišík M, Condon DJ, McInnes BIA, Jaques AL and Evans NJ** (2023) Emplacement of the Argyle diamond deposit into an ancient rift zone triggered by supercontinent breakup. *Nature Communications* **14**, 5274.

**Olierook HKH, Rankenburg K, Ulrich S, Kirkland CL, Evans NJ, Brown S, McInnes BIA, Prent A, Gillespie J, McDonald B and Darragh M** (2020) Resolving multiple geological events using in situ Rb–Sr geochronology: implications for metallogenesis at Tropicana, Western Australia. *Geochronology* **2**, 283–303.

**Olierook HK, Agangi A, Plavsa D, Reddy SM, Yao W, Clark C, Occhipinti SA and Kylander-Clark AR** (2019) Neoproterozoic hydrothermal activity in the West Australian Craton related to Rodinia assembly or breakup? *Gondwana Research* **68**, 1–12.

**Oliveira ÍL, Brod JA, Cordeiro PFO, Dantas EL and Mancini LH** (2017) Insights into the late-stage differentiation processes of the Catalão I carbonatite complex in Brazil: new Sr–Nd and C–O isotopic data in minerals from niobium ores. *Lithos* **274**, 214–24.

**Piazolo S, Daczko NR, Silva D and Raimondo T** (2020) Melt-present shear zones enable intracontinental orogenesis. *Geology* **48**, 643–48.

**Pidgeon RT, Smith CB and Fanning CM** (1989) Kimberlite and lamproite emplacement ages in Western Australia. *Kimberlites and Related Rocks* **1**, 382–91.

**Pirajno F, González-Álvarez I, Chen W, Kyser KT, Simonetti A, Leduc E and leGras M** (2014) The Gifford Creek Ferrocarbonatite Complex, Gascoyne Province, Western Australia: associated fenitic alteration and a putative link with the ~1075 Ma Warakurna LIP. *Lithos* **202–203**, 100–19.

**de Gromard QR, Kirkland CL, Howard HM, Wingate MT, Jourdan F, McInnes BI, Danišík M, Evans NJ, McDonald BJ and Smithies RH** (2019) When will it end? Long-lived intracontinental reactivation in central Australia. *Geoscience Frontiers* **10**, 149–64.

**Ribeiro BV, Lagoeiro L, Faleiros FM, Hunter N, Queiroga G, Raveggi M, Cawood PA, Finch M and Campanha G** (2020) Strain localization and fluid-assisted deformation in apatite and its influence on trace elements and U–Pb systematics. *Earth and Planetary Science Letters* **545**, 116421.

**Ribeiro BV, Kirkland CL, Kelsey DE, Reddy SM, Hartnady MIH, Faleiros FM, Rankenburg K, Liebmann J, Korhonen FJ and Clark C** (2023) Time-strain evolution of shear zones from petrographically constrained Rb–Sr muscovite analysis. *Earth and Planetary Science Letters* **602**, 117969.

**Rösel D and Zack T** (2022) LA-ICP-MS/MS single-spot Rb-Sr dating. *Geostandards and Geoanalytical Research* **46**, 143–68.

**Schulz KJ, Piatak NM, Papp JF, DeYoung JH, Seal RR and Bradley DC** (2017) *Niobium and Tantalum; Chapter M of Critical Mineral Resources of the United States—Economic and Environmental Geology and Prospects for Future Supply*. Reston, VA: U.S. Geological Survey.

**Scrimgeour IR, Kinny PD, Close DF and Edgoose CJ** (2005) High-T granulites and polymetamorphism in the southern Arunta Region, central Australia: evidence for a 1.64 Ga accretional event. *Precambrian Research* **142**, 1–27.

**Simpson A, Glorie S, Hand M, Spandler C, Gilbert S and Cave B** (2022) In situ Lu–Hf geochronology of calcite. *Geochronology* **4**, 353–72.

**Simpson A, Gilbert S, Tamblyn R, Hand M, Spandler C, Gillespie J, Nixon A and Glorie S** (2021) In-situ Lu Hf geochronology of garnet, apatite and xenotime by LA ICP MS/MS. *Chemical Geology* **577**, 120299.

**Slezak P and Spandler C** (2019) Carbonatites as recorders of mantle-derived magmatism and subsequent tectonic events: an example of the Gifford Creek Carbonatite Complex, Western Australia. *Lithos* **328–329**, 212–27.

**Spencer CJ, Kirkland CL, Roberts N, Evans NJ and Liebmann J** (2020) Strategies towards robust interpretations of in situ zircon Lu–Hf isotope analyses. *Geoscience Frontiers* **11**, 843–53.

**Stracke A** (2012) Earth's heterogeneous mantle: a product of convection-driven interaction between crust and mantle. *Chemical Geology* **330**, 274–99.

**Sudholz ZJ, Reddicliffe TH, Jaques AL, Yaxley GM, Haynes M, Gorbatov A, Czarnota K, Frigo C, Maas R and Knowles B** (2023) Petrology, age, and rift origin of ultramafic lamprophyres (aillikites) at Mount Webb, a new alkaline province in Central Australia. *Geochemistry, Geophysics, Geosystems* **24**, e2023GC011120.

**Sykes LR** (1978) Intraplate seismicity, reactivation of preexisting zones of weakness, alkaline magmatism, and other tectonism postdating continental fragmentation. *Reviews of Geophysics* **16**, 621–88.

**Tappe S, Stracke A and Yaxley GM** (2024) The sources of economic carbonatites through time. *2024 Goldschmidt Conference*, Chicago, United States, 18–23 August 2024.

**Tappe S, Stracke A, van Acken D, Strauss H and Luguet A** (2020) Origins of kimberlites and carbonatites during continental collision–insights beyond decoupled Nd-Hf isotopes. *Earth-Science Reviews* **208**, 103287.

**Tappe S, Pearson DG, Nowell G, Nielsen T, Milstead P and Muehlenbachs K** (2011) A fresh isotopic look at Greenland kimberlites: cratonic mantle lithosphere imprint on deep source signal. *Earth and Planetary Science Letters* **305**, 235–48.

**Tappe S, Foley SF, Stracke A, Romer RL, Kjarsgaard BA, Heaman LM and Joyce N** (2007) Craton reactivation on the Labrador Sea margins: 40Ar/39Ar age and Sr–Nd–Hf–Pb isotope constraints from alkaline and carbonatite intrusives. *Earth and Planetary Science Letters* **256**, 433–54.

**Tappe S, Foley SF, Jenner GA, Heaman LM, Kjarsgaard BA, Romer RL, Stracke A, Joyce N and Hoefs J** (2006) Genesis of ultramafic lamprophyres and carbonatites at Aillik Bay, Labrador: a consequence of incipient lithospheric thinning beneath the North Atlantic Craton. *Journal of Petrology* **47**, 1261–315.

**Vance D, Müller W and Villa IM** (2003) Geochronology: linking the isotopic record with petrology and textures—an introduction. *Geological Society, London, Special Publications* **220**, 1–24.

**WA1 Resources** (2025) *West Arunta Project – Indicated Mineral Resource Estimate for Luni: ASX Release, 30 June 2025*. Subiaco, WA: WA1 Resources Ltd.

**WA1 Resources** (2024) *West Arunta Project – Mineral Resource Estimate for Luni: ASX Release, 1 July 2024*. Subiaco, WA: WA1 Resources Ltd.

**WA1 Resources** (2022a) *Discovery of Niobium-REE Mineralised Carbonatite System: ASX Release, 26 October 2022*. Subiaco, WA: WA1 Resources Ltd.

**WA1 Resources** (2022b) *Discovery of a Second Niobium-REE Mineralised carbonatite System at Luni: ASX Release, 16 November 2022*. Subiaco, WA: WA1 Resources Ltd.

**Wade BP, Barovich KM, Hand M, Scrimgeour IR and Close DF** (2006) Evidence for early Mesoproterozoic arc magmatism in the Musgrave Block, central Australia: implications for Proterozoic crustal growth and tectonic reconstructions of Australia. *The Journal of Geology* **114**, 43–63.

**Walsh AK, Raimondo T, Kelsey DE, Hand M, Pfitzner HL and Clark C** (2013) Duration of high-pressure metamorphism and cooling during the intraplate Petermann Orogeny. *Gondwana Research* **24**, 969–83.

**Wang XC, Li XH, Li ZX, Liu Y and Yang YH** (2010) The Willouran basic province of South Australia: its relation to the Guibei large igneous province in South China and the breakup of Rodinia. *Lithos* **119**, 569–84.

**Watson EB and Green TH** (1981) Apatite/liquid partition coefficients for the rare earth elements and strontium. *Earth and Planetary Science Letters* **56**, 405–21.

**Williams-Jones AE and Vasyukova OV** (2023) Niobium, critical metal, and progeny of the mantle. *Economic Geology* **118**, 837–55.

**Williams-Jones AE and Migdisov AA** (2014) Experimental constraints on the transport and deposition of metals in ore-forming hydrothermal systems. In *Building Exploration Capability for the 21st Century* (eds KD Kelley and HC Golden). McLean: GeoScience World.

**Wingate MTD, Fielding I, Kelsey DE, Turnbull RE and Lu Y** (2024) *262476.1: Lamprophyre Dyke, Crean Prospect*. Perth: Geological Survey of Western Australia.

**Wingate MTD, Lu Y, Fielding I, Kelsey DE and Spaggiari CV** (2022) *243061: Siliciclastic Schist, Radiator Prospect*. Perth: Geological Survey of Western Australia.

**Wingate MTD, Campbell IH, Compston W and Gibson GM** (1998) Ion microprobe U–Pb ages for Neoproterozoic basaltic magmatism in south-central Australia and implications for the breakup of Rodinia. *Precambrian Research* **87**, 135–59.

**Wu L, Liu Y, Wang F, Zeng L, Yang L, Tian Y and Zhang W** (2017) Cretaceous exhumation of Proterozoic carbonatite on the northern margin of the North China Craton constrained by apatite fission-track and (U-Th)/He geochronology. *Chemical Geology* **125**, 593–606.

**Xue G, Zhang J, Chen W, Wu X, Wang J, Di Q, Xu Y, Zhao Y, Li X, Zhao Y and Mitchell R** (2024) Translithospheric carbonatite magmatic system of the world's largest REE deposit, Bayan Obo, China. *Geology* **53**, 119–24.

**Yang X, Lai X, Pirajno F, Liu Y, Mingxing L and Sun W** (2017) Genesis of the Bayan Obo Fe-REE-Nb formation in Inner Mongolia, North China Craton: a perspective review. *Precambrian Research* **288**, 39–71.

**Yang Y-H, Wu F-Y, Yang J-H, Chew DM, Xie L-W, Chu Z-Y, Zhang Y-B and Huang C** (2014) Sr and Nd isotopic compositions of apatite reference materials used in U–Th–Pb geochronology. *Chemical Geology* **385**, 35–55.

**Yaxley GM, Anenburg M, Tappe S, Decree S and Guzmics T** (2022) Carbonatites: classification, sources, evolution, and emplacement. *Annual Review of Earth and Planetary Sciences* **50**, 261–93.

**Zametzer A, Kirkland CL, Barham M, Hartnady MI, Bath AB and Rankenburg K** (2022) Episodic alteration within a gold-bearing Archean shear zone revealed by in situ biotite Rb–Sr dating. *Precambrian Research* **382**, 106872.

**Zhang C-L, Li X-H, Li Z-X, Lu S-N, Ye H-M and Li H-M** (2007) Neoproterozoic ultramafic–mafic–carbonatite complex and granitoids in Quruqtagh of northeastern Tarim Block, western China: geochronology, geochemistry and tectonic implications. *Precambrian Research* **152**, 149–69.

**Zhao J and McCulloch MT** (1993) Sm-Nd mineral isochron ages of Late Proterozoic dyke swarms in Australia: evidence for two distinctive events of mafic magmatism and crustal extension. *Chemical Geology* **109**, 341–54.

**Zhou M-F, Kennedy AK, Sun M, Malpas J and Lesher CM** (2002) Neoproterozoic arc-related mafic intrusions along the northern margin of South China: implications for the accretion of Rodinia. *Journal of Asian Earth Sciences* **110**, 611–18.

**Zozulya DR, Kullerud K, Ribacki E, Altenberger U, Sudo M and Savchenko YE** (2020) The newly discovered Neoproterozoic aillikite occurrence in Vinoren (Southern Norway): age, geodynamic position and mineralogical evidence of diamond-bearing mantle source. *Minerals* **10**, 1029.